NEOARCHEAN DEPOSITION, METAMORPHISM, AND INTRUSION IN RAPID SUCCESSION, VERMILION GRANITIC COMPLEX, SUPERIOR PROVINCE OF NORTHERN MINNESOTA

A THESIS SUBMITTED TO THE FACULTY OF
THE GRADUATE SCHOOL OF THE UNIVERSITY OF MINNESOTA
BY

ROSS A. SALERNO

IN PARTIAL FULFILLMENT OF THE REQUIREMENTS
FOR THE DEGREE OF
MASTER OF SCIENCE

ADVISOR: JOHN W. GOODGE

JULY, 2017

Acknowledgments

This project is the summation of a number of hours, days, weeks, and months of research over the past 2 years. Completion would not have been possible without support from a number of individuals. I would like to thank my advisor, Dr. John Goodge for his countless hours of council and mentorship. My committee members Dr. Vicki Hansen and Dr. Paul Siders contributed by refining the aim of this work. Fieldwork would have been far more arduous and lonesome without the help of Catherine Hafdahl and Tyler Untiedt. I have been so fortunate during this project to rely on my fellow Duluth students for comradery, commiseration, and morale. Ultimately my family, whom without none of this would be. This document is dedicated in memorial to my grandmothers: Carmella Salerno, who passed during the synthesis of this work, and Danielle Garrison, who gave me so much.

Table of contents

List of tables

List of figures

List of mineral abbreviations

Ab	-	Albite
Alm	-	Almandine
And	-	Andalusite
Ann	-	Annite
An	-	Anorthite
Bt	-	Biotite
Cld	-	Chloritoid
Grt	-	Garnet
Kfs	-	Potassium feldspar
Ky	-	Kyanite
Ms	-	Muscovite
Mz	-	Monazite
Or	-	Orthoclase
Qtz	-	Quartz
Sil	-	Sillimanite
Zrn	-	Zircon

1 Introduction

Petrologic, structural, and geochemical study of Archean rocks fosters much debate about the nature of early Earth geodynamics. Crustal assembly mechanisms over long geologic time scales are temporally dependent on evolving mantle and lithosphere thermo-mechanical processes (Martin, 1994; Hawkesworth and Kemp, 2006; Rey and Houseman, 2006; Ernst et al., 2016). These processes were likely very different in early Earth history relative to today. In particular, the Archean is a period when crustal preservation time significantly lengthened, mantle overturn rates diminished, and crust thickened, cooled, and strengthened (Anderson, 1987; Condie and Kroner, 2013). Crustal changes appear to have culminated in the Neoarchean, signifying a threshold in the net growth of crust through time. Net crustal growth is quantified as the difference between crustal production and destruction (Ernst et al., 2016). On the basis of global isotopic and age datasets, the net growth of crust in the Neoarchean, at ~ 2.7 Ga, is estimated to be greater than any other time in Earth history (Condie, 2007; Condie and Kroner, 2013).

The Meso- to Neoarchean belts of the Superior province in North America are representative of this transitional period in geologic time. The Superior province forms the cratonic core of North America and is the largest exposed section of Archean crust (4.0 – 2.5 Ga) on Earth. Alternating belts of high-grade granite-gneiss and low-grade metavolcanosedimentary granite-greenstone are characteristic of Archean cratons (Condie, 1994). In the Superior province belts strike northeast and define subprovinces on the basis of structural trends and lithologic variation (Figure 1; Card and Ciesielski, 1985; Williams, 1991). Among these, the Neoarchean Wabigoon, Quetico, and Wawa subprovinces constitute the Superior province in northern Minnesota (Thurston, 1991; Easton, 2000).

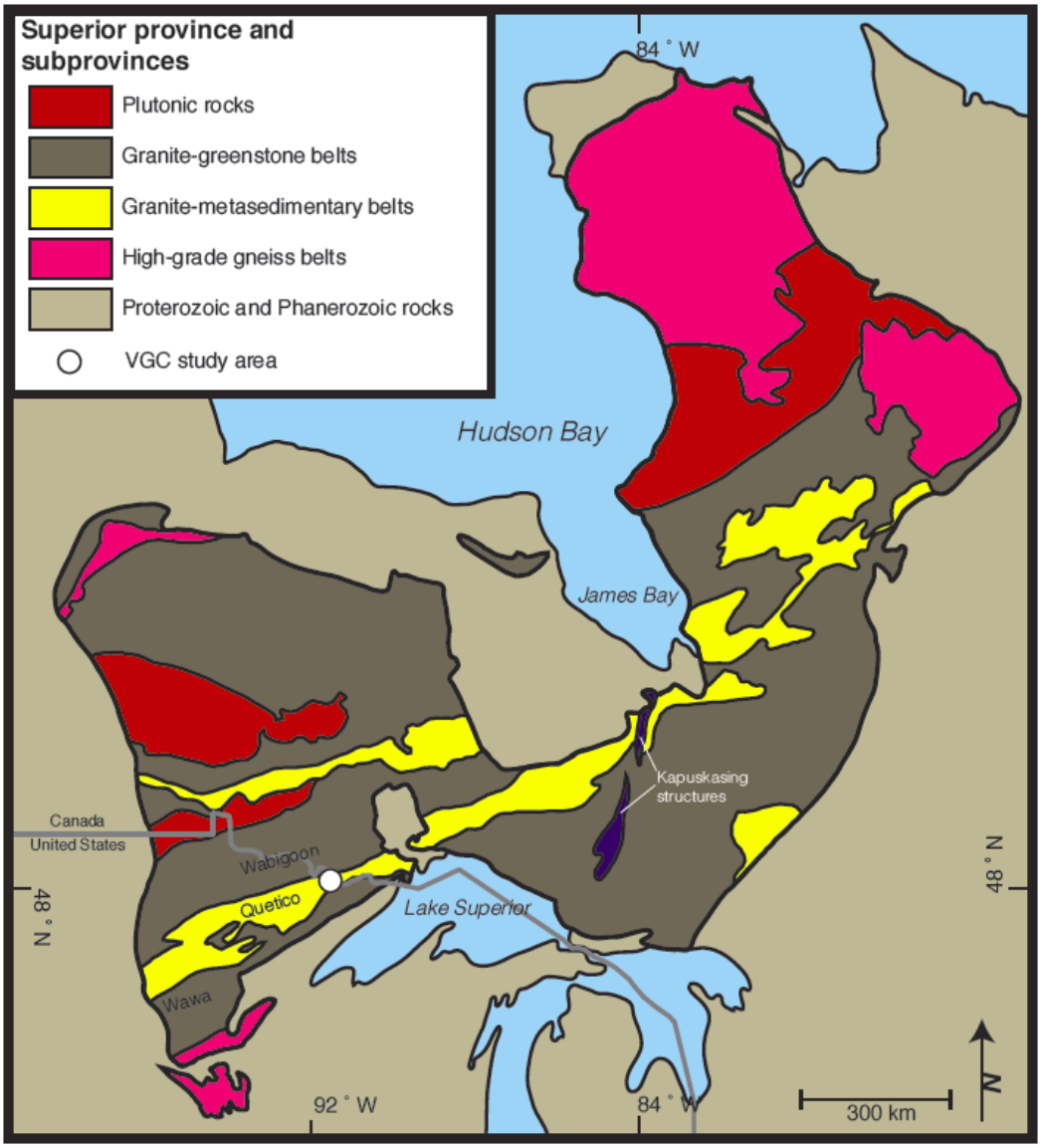

Figure 1. Subprovinces of the Superior province, after Card and Ciesielski (1986). Note the location of the Vermilion Granitic Complex study area shown in Figure 2, within the Quetico metasedimentary belt.

Petrologic and geochronologic study of Quetico subprovince igneous and metamorphic rocks can provide an understanding of the mechanisms and rates of crustal evolution during the Neoarchean transition. Igneous rocks record geochemical interactions during melting, and provide age constraints on melt emplacement and deformation. Likewise, metamorphic pressure-temperature-time (P-T-t) reconstructions constrain the conditions and tempo of crustal evolution. Such P-T-t constraints depend on aluminous metamorphic assemblages and accessory mineral phases, useful in estimating P-T paths and determining isotopic ages, respectively. In many cases, however, Archean rocks lack the required aluminous and accessory assemblages because the accumulation of true pelitic sediments was uncommon along the margins of small Archean protocontinents (Condie, 1981; Ojakangas, 1985). Thus, the bulk composition of the common Archean metagreywacke and metavolcanosedimentary rocks produced few phases and reactions useful for P-T-t reconstructions (Condie 1998). Exceptionally, metamorphic rocks in the Quetico subprovince of the Superior province locally host a number of key aluminous phases, reactions, and accessory minerals facilitating study of the formation and metamorphic evolution of this Neoarchean terrain (Southwick and Sims, 1980; Day and Weiblen, 1986; Tabor, 1991; Pan and Fleet, 1999).

In this study I focus on an area of the western Quetico belt defined as the Vermilion Granitic Complex (VGC). I employ field observations, petrography, mineral chemistry, geothermometry, and geochronology to explore the conditions and timing associated with the evolution of the VGC. Field relationships between igneous and metamorphic rock units illustrate a multiphase plutonic and migmatite formation history. Conditions of metamorphism, mode of migmatite formation, and U-Pb geochronologic age constraints

on monazite and zircon provide insight into the inter-related processes that led to the development of the VGC. New field, petrologic, and geochronologic data indicate the formation of the VGC by: 1) co-development of plutonic sediment provenance and a proximal depositional basin, 2) metamorphism of basinal sediments, 3) syn- to post-metamorphic injections of granitic melt, and 4) the injection driven formation of migmatite schist-granitoid structures. These events occurred in rapid succession, with a total deposition-metamorphism-plutonism interval as brief as ~ 30 Ma.

2 Background

The Vermilion Granitic Complex is located in the western region of the Quetico subprovince (Figure 2, Figure 3). The Rainy Lake-Seine River Fault defines the northern margin of the VGC as the border between the Quetico belt and Wabigoon greenstone belt. The Vermilion Fault marks the southern margin of the complex as the border between the Quetico belt and Wawa greenstone belt (Southwick and Ojakangas, 1979; Southwick and Sims, 1980). The complex encompasses an area of ~ 6,500 km^2 of the western Quetico belt.

Country rock in the VGC is a biotite ± muscovite ± garnet ± sillimanite schist, and hosts multiple phases of granitic rocks (Day, 1983; Tabor, 1988; Percival, 1988). Table 1 lists the representative units comprising the VGC. The occurrence of aluminous metamorphic assemblages in schist is local, resulting from the metamorphism of a compositionally-variable precursor consisting of greywacke and argillite interbeds. Compositions of protolith interbeds ranged from clay-rich semi-pelites to volcanosedimentary feldspathic arenites, metamorphosed to assemblages of garnet-mica and biotite-amphibole, respectively (Day, 1983).

The core of the VGC is characterized by a large, kilometer-scale body of the Lac La Croix Granite (LLCG; Poulsen et al., 1980). A low initial $^{87}Sr / ^{86}Sr$ value for the LLCG indicates a deep crust or mantle melt source (Peterman et al., 1972). Granitic bodies of smaller volume occur throughout the complex, and range in composition from granodiorite to leucogranite (Southwick, 1972). Day (1983) and Day and Weiblen (1986) illustrated geochemical similarities between the biotite schist and leucogranitic rocks in the VGC and proposed country rock anatexis as a likely source of melt. The VGC hosts a variety of

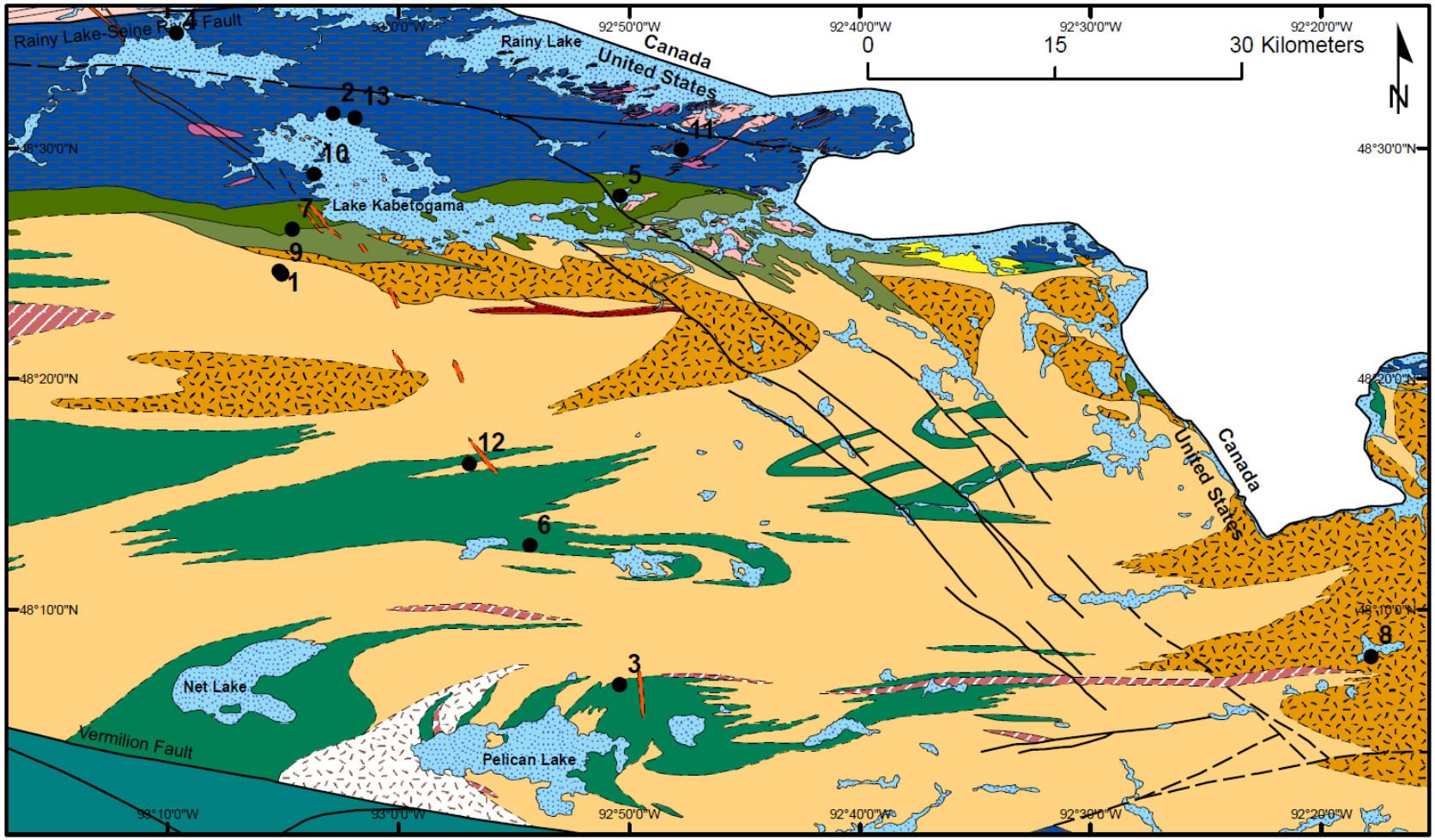

Figure 2. General geology of the Vermilion Granitic Complex in northern Minnesota. Symbology explained in Figure 3. Modified from Southwick and Ojakangas (1979) and Hemstad et al. (2002).

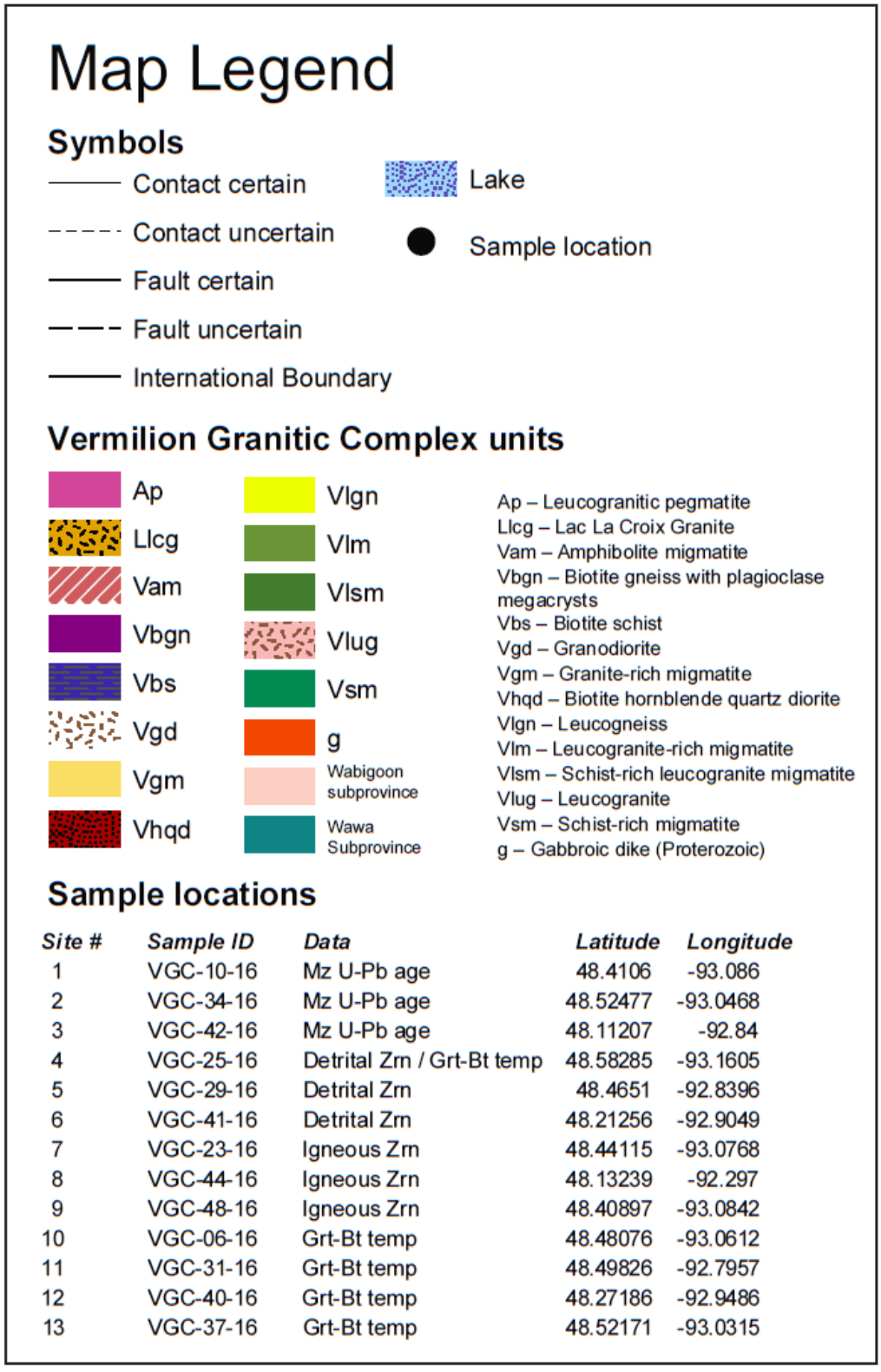

Site #	*Sample ID*	*Data*	*Latitude*	*Longitude*
1	VGC-10-16	Mz U-Pb age	48.4106	-93.086
2	VGC-34-16	Mz U-Pb age	48.52477	-93.0468
3	VGC-42-16	Mz U-Pb age	48.11207	-92.84
4	VGC-25-16	Detrital Zrn / Grt-Bt temp	48.58285	-93.1605
5	VGC-29-16	Detrital Zrn	48.4651	-92.8396
6	VGC-41-16	Detrital Zrn	48.21256	-92.9049
7	VGC-23-16	Igneous Zrn	48.44115	-93.0768
8	VGC-44-16	Igneous Zrn	48.13239	-92.297
9	VGC-48-16	Igneous Zrn	48.40897	-93.0842
10	VGC-06-16	Grt-Bt temp	48.48076	-93.0612
11	VGC-31-16	Grt-Bt temp	48.49826	-92.7957
12	VGC-40-16	Grt-Bt temp	48.27186	-92.9486
13	VGC-37-16	Grt-Bt temp	48.52171	-93.0315

Figure 3. Symbology used in Figure 2, with locations of samples used for geochronology and garnet-biotite temperatures.

Table 1. Major lithologies of the Vermilion Granitic Complex.

Unit	Lithology	Representative sample	Latitude	Longitude	U-Pb Age
Biotite schist	Biotite-garnet-sillimanite schist	VGC-25-16	48.58585	-93.16047	~ 2675 Ma
Leucogranite	Biotite-muscovite granite	VGC-23-16	48.44115	-93.07676	2708 Ma ± 94
Lac La Croix Granite	Biotite-magnetite granite	VGC-44-16	48.13239	-92.29695	2668 Ma ± 10
Granodiorite	Granodiorite	VGC-48-16	48.40891	-93.08384	2684 Ma ± 23

migmatites; stromatic, rafted, and veined types (see Mehnert, 1968 and Sawyer, 2008 for descriptions). Migmatitic and schistose country rock occur proximal to the margins of the VGC, whereas the core of the complex is largely granite and granite-rich migmatite.

Percival and Sullivan (1988) reported zircon, monazite, and titanite U-Pb ages of Quetico plutonic and metagreywacke rocks east of the VGC, near Lappe, Ontario. Metasupracrustal zircons are detrital in origin, with the youngest grain at 2702 ± 4 Ma constraining the maximum age of protolith deposition. Zircon and monazite U-Pb ages date a granodiorite cross-cutting biotite schist and biotite-granite at 2687 ± 9 Ma and 2665 ± 2 Ma, respectively. Davis et al. (1990) establish a similar maximum age of protolith deposition at 2689 ± 3 Ma with the youngest detrital zircon in Quetico supercrustals near Atikokan, Ontario. Their work also reports the age of the granitic Blalock pluton, observed to cross-cut the Quetico metasupracrustals at 2688 ± 4 Ma.

3 Methods

3.1 Field Methods

My field work during the summer of 2016 fieldwork was carried out in areas of Voyagers National Park, Superior National Forest, Kabetogama State Forest, and the Boundary Waters Canoe Area Wilderness (BWCAW). The National Park Service granted permits for work in Voyagers National Park, and the National Forest Service permitted work in Superior National Forest and the BWCAW.

Due to the scale of the scale, degree of vegetation, and remoteness of the field area I constructed a preliminary sampling plan based on the field observations of Southwick and Ojakangas (1979), Tabor (1988), and Hemstad et al. (2002). This plan targeted the major lithologies in the complex for sampling. I configured VGC metasupracrustal sample sites regionally to best explore for possible metamorphic field isograds. To place absolute age constraints on plutonic-metasupracrustal rock field relationships, I sampled the three main granitic phases in the VGC for later geochronology.

I made observations at road cuts, outcrops in logged areas and forest burns, active quarries, and on lakeshore exposures. My field descriptions of schist country rock noted the presence and composition of any granitic dikes, the degree of foliation, mineralogy, and the presence of compositional layering or relict bedding. I classified migmatites by structural type (in the schemes of Mehnert, 1969 and Sawyer, 2008), paleosome mineralogy, the degree of paleosome foliation, and neosome lithology. My descriptions of granitic rocks record lithology and the unit's textural relationship with the country rock.

I collected approximately 5 kg of each lithology at sites for thin section preparation and potential accessory mineral geochronology. In the case of migmatized rocks, I sampled

both leucosomal and melanosomal material. Ultimately, the 46 samples collected represent the major units in the VGC: biotite schist country rock, Lac La Croix granite (LLCG), leucogranite, and granodioritic-tonalitic rocks. See Appendix A for sample locations and field descriptions.

3.2 Thin section petrography

I prepared 44 thin sections for a geographically and lithologically representative set of schist and granitic samples. I cut sections parallel to rock lineation and perpendicular to rock foliation. All sections were polished suitable for microprobe analyses.

My transmitted-light petrographic descriptions note the degree of foliation, framework mineralogy, modal mineralogy, reaction textures, metamorphic assemblages, and the presence of index minerals such as aluminosilicate. I selected samples with garnetiferous assemblages for garnet compositional analyses and garnet-biotite thermometry. I identified monazite and zircon in schist samples, as well as zircons in granitic samples for later age dating.

3.3 Scanning Electron Microscope analyses

I used the JEOL JSM-6490 LV scanning electron microscope at the University of Minnesota, Duluth for imaging and compositional analyses. The instrument was equipped with an Oxford Inca x-act energy-dispersive spectroscopy (EDS) X-ray detector for qualitative compositional analyses. Backscattered electron (BSE) imaging and EDS analyses were obtained at an accelerating voltage of 15 kV and beam diameter < 1 μm. I

used EDS and BSE imaging to further characterize monazite and zircon in biotite schist samples to examine the textural context of these phases within the metamorphic fabric.

I explored garnet zonal compositional variation with EDS line profiles. Each line profile consisted of 20 spot analyses equally spaced across a transect line. Elemental weight percentages of Fe, Mg, Ca, and Mn are reported for each analytical spot along the profile.

3.4 Electron microprobe chemical analyses

Mineral chemical analyses were performed using the electron probe microanalyser (EPMA) at the University of Minnesota, Twin Cities Electron Microprobe Lab. I characterized garnet, biotite, and monazite chemistry from thin sections by wavelength dispersive spectroscopy (WDS) on a JEOL JXA-8900R electron microprobe. Operating conditions for all analyses were: accelerating voltage of 15 kV, beam current of 20 nA, and beam diameter < 1 micron. Elements were measured using Li FH crystal for Mn and Fe; PETJ for Ca, Ti, Cr, K, and Cl; and TAP for Al, Mg, Na, Si, and Mg. The off-peak correction method was linear for all elements. Unknown and standard intensities were corrected for deadtime. Standard intensities were corrected for standard drift over time. Appendix B lists the standards used for peak calibrations.

3.5 Mineral separation

Zircon separates were processed from schist and granitic samples; monazite separates were processed from schist samples. ZirChron LLC of Tucson, AZ performed all mineral separations. Electronic pulse disaggregation reduced hand samples to grain sizes of sand and smaller. Sieving isolated grain-size fractions between 250 μm and 50 μm.

Mineral separates with densities greater than 3.3 g/cm^3 and with magnetic resonance between 0.4 - 0.7 amperes concentrated monazite. Separates with densities greater than 3.3 g/cm^3 and non-magnetic at 0.4 amperes concentrated zircon.

3.6 Laser ablation inductively coupled plasma mass spectrometry

I hand-picked crack and inclusion free zircons under a stereoscopic microscope from mineral separates. I mounted grains in 7/8-inch round epoxy pucks for in-situ laser ablation inductively coupled plasma mass spectrometry (LA-ICPMS) analyses. I polished pucks to expose approximately half of each embedded zircon grain. Cathodoluminescence (CL) imaging of epoxy-mounted zircons prior to laser ablation revealed compositional heterogeneities within zircons and guided laser spot analyses towards only homogenous growth domains. I mapped Ce, La, and REE compositions for monazites in thin section by EPMA to constrain age heterogeneities within monazite grains.

I conducted isotopic analyses at the Radiogenic Isotope and Geochronology Laboratory at Washington State University. U-Th-Pb were collected on a Thermo Element 2 ICPMS for zircon and monazite. I analyzed biotite schist zircons at a laser spot size of 20 μm, laser frequency of 10 Hz, and 10 J/cm^2 laser power. I used the same settings to analyze biotite schist monazites, except at an 8 μm spot size. I collected U-Th-Pb and Hf on zircons from granitic rocks in split stream configuration with a Thermo Element 2 (for U-Th-Pb) and a Thermo Neptune (for Hf) at a spot size of 40 μm, laser frequency of 10 Hz, and 10 J/cm^2 laser power. Appendix C lists age correction standards.

4 Major lithologies

The VGC is comprised of metamorphic country rock that hosts a variety of granitic phases, which occur as the mappable units of both the margins and the interior of the complex (Figure 2). Migmatites characterize the interface between country rock and granitoids, accounting for approximately 40% of total exposed VGC geology. Migmatite is a term to describe lithologies incorporating two macroscopically distinct, but physically mixed components of igneous and/or metamorphic rock. Migmatitic textures intimately juxtapose darker, mafic, and often metamorphic material (melanosome) with lighter, felsic, and more coarsely grained igneous components (leucosome). The melanosome of VGC migmatite is ubiquitously the biotite schist country rock, with leucosome lithology varying in composition from leucogranitic to tonalitic.

4.1 Metamorphic country rock

The country rock of the VGC is a foliated, lepidoblastic biotite schist. Biotite schist flanks the complex to the north and west. Exposures of the schist are common on the shores of the Kabetogama peninsula and of Rainy Lake in areas east of International Falls.

In outcrop, the schist has a grey to brown-grey color. Advanced alteration-oxidation of mafic phases results in a dark grey to black surface. Lithologic heterogeneity is evident by mineralogically distinct horizons on a scale of centimeters to decimeters (Figure 4). These layers are thought to be primary, indicating the protolith consisted of argillaceous, arenitic, and volcanosedimentary interbedded sediments. Meta-argillite horizons host assemblages of metamorphic biotite ± muscovite ± sillimanite ± garnet. Meta-arenite horizons are muscovite poor, mainly composed of biotite + quartz + plagioclase.

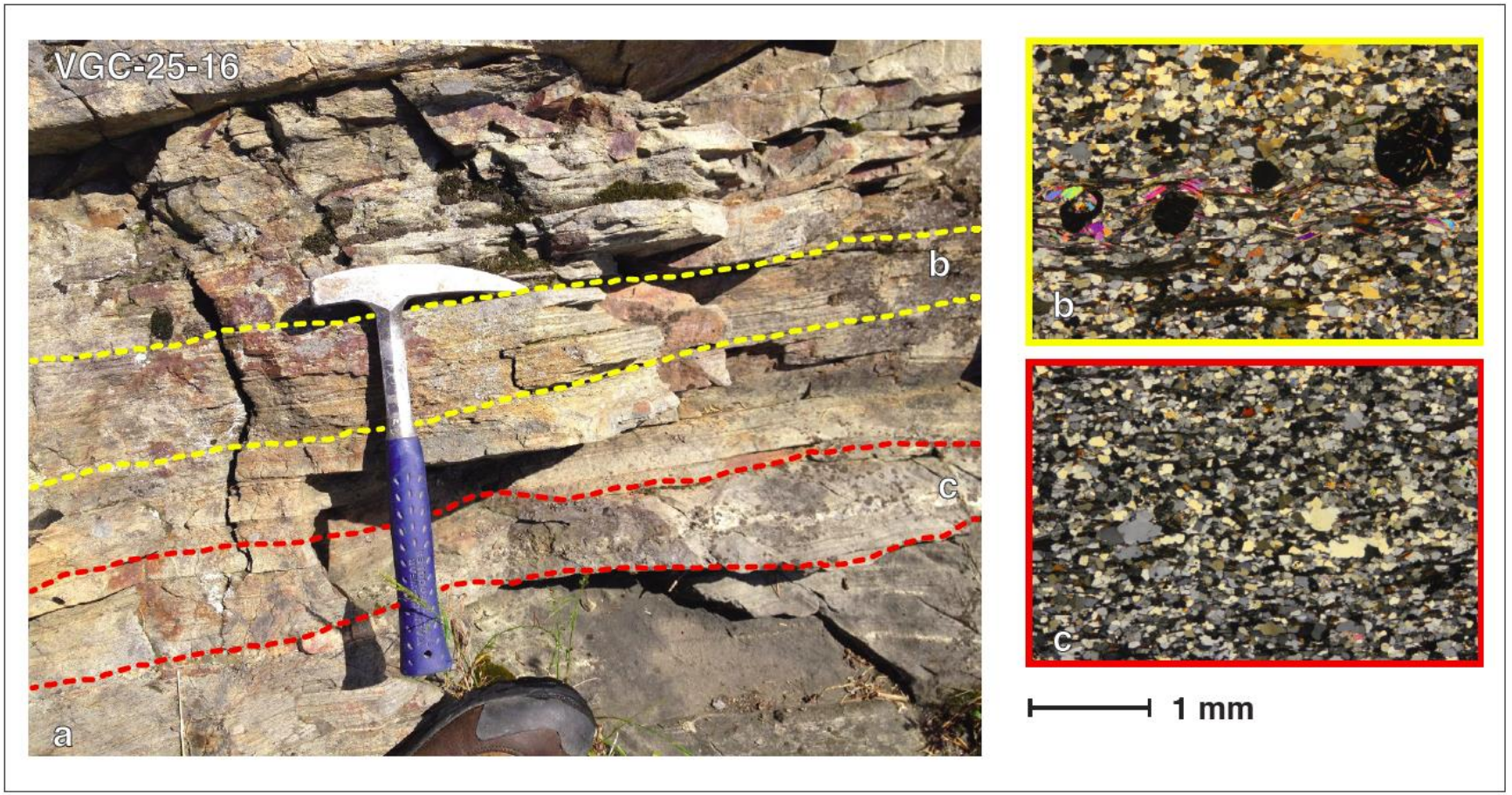

Figure 4. (a) Compositional variability of the biotite schist at outcrop scale. (b) In yellow, aluminous meta-argillite horizons with distinct garnet and muscovite assemblages. (c) In red, arenitic horizons are composed mainly of quartzofeldspathic framework minerals with a foliation defined by biotite.

amphibole-rich metamorphic assemblages are localized to metavolcanosedimentary horizons. The degree of foliation development in the biotite schist is variable throughout the VGC and is related to changes in biotite abundance and grainsize.

Petrographically, quartz and plagioclase constitute the framework mineralogy of the biotite schist. Quartz is fine to medium grained (0.25 to 0.5 mm) and slightly elongate within the foliation fabric of the rock. Undulose extinction characterizes larger quartz grains. Inclusions of quartz are common in albite, garnet, and microcline poikiloblasts. Plagioclase grains are angular and compositionally albitic, averaging An_{30} (determined by the Michel-Lèvy method and by EDS spot analyses). Seritization of plagioclase is common, with advanced seritization concentrated proximal to quartz veining.

The occurrence of alkali feldspar is limited in the VGC. Microcline grain types occur as both fine grained (0.1 to 0.2 mm) and porphyroblastic (~ 1.25 mm). Porphyroblasts are poikiloblastic and host inclusions of quartz, albite, muscovite, and biotite (Figure 5a). Poikiloblasts are anhedral with irregular boundaries. The modal abundance of alkali feldspar does not exceed 5% at the few localities where it occurs.

Medium- to fine-grained biotite defines the lepidoblastic foliation of the schist country rock. Variation in the degree of foliation development is dependent on biotite grain size and modal abundance. In weakly foliated schist, biotite laths range from 0.85 to 1.0 mm in length and constitute approximately 20% of modal mineralogy. Larger and thicker laths of about 4.0 mm length constitute 35% of modal mineralogy in strongly foliated schist. The average composition of biotite is 52% annite (determined by EPMA spot analyses).

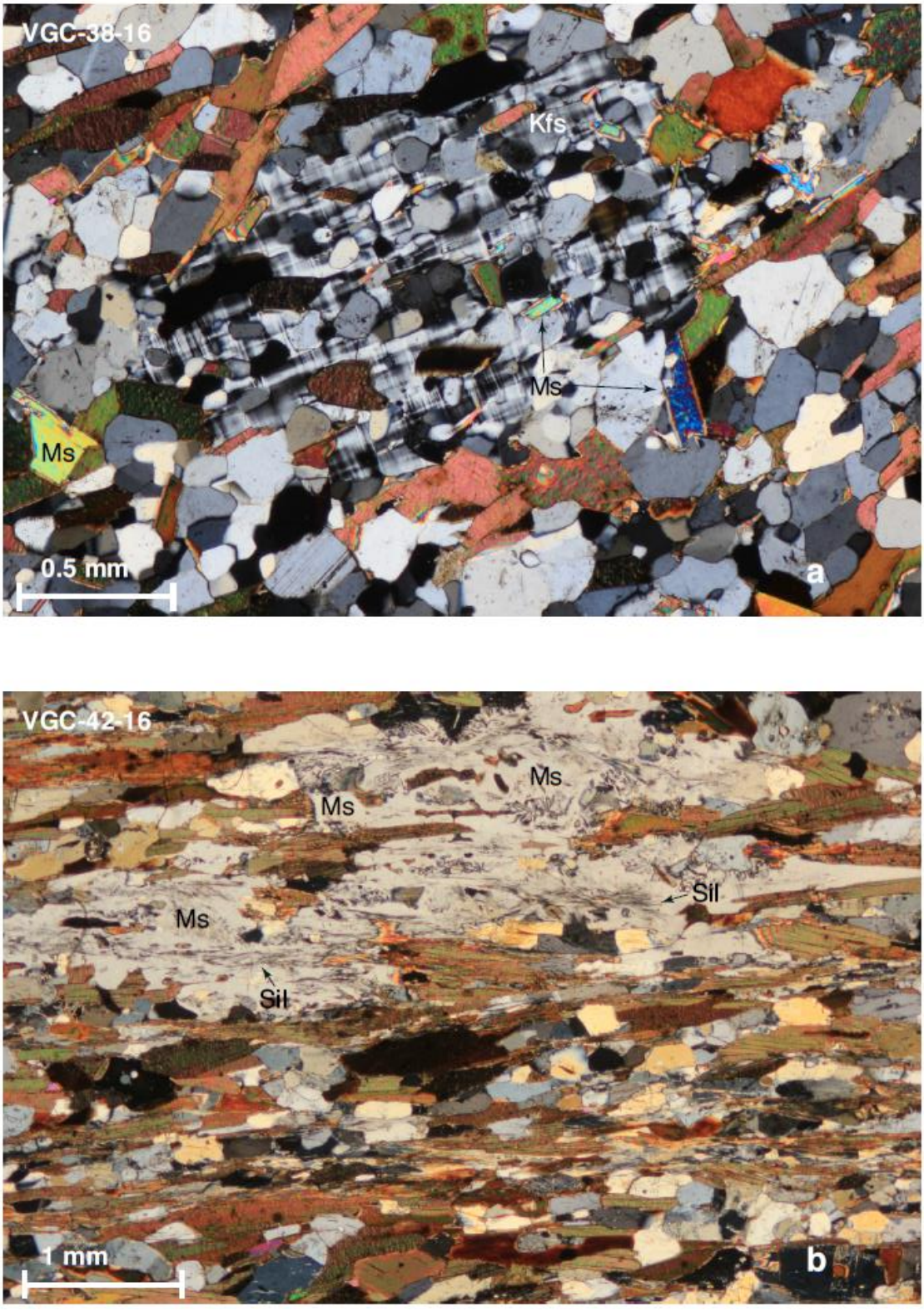

Figure 5. Photomicrographs of representative biotite schist, showing (a) poikiloblastic microcline prophyroblast, and (b) symplectic M1b muscovite with fibrolitic sillimanite.

Three textural classes of muscovite are distinguished on the basis of grain size, petrographic context, and crystal form. M1a muscovite is the oldest discernable generation of metamorphic muscovite. M1a crystals are anhedral and enveloped by fibrolitic sillimanite mats. Grain boundaries between M1a muscovite and sillimanite are irregular and difficult to distinguish optically. M1b muscovite is euhedral and intergrown symplectically with quartz and plagioclase. M1b muscovite hosts fibrolitic sillimanite needles, and these phases texturally appear to be coeval (Figure 5b). M1b muscovite porphyroblasts range in size from 0.75 – 1.0 mm. The occurrence of M1b muscovite is confined to aluminous meta-argillite horizons in the biotite schist. M2 is the latest generation of muscovite and occurs as a retrograde or post-metamorphic product of advanced seritization of plagioclase.

Sillimanite is the only Al_2SiO_5 polymorph found during this study and occurs locally in metasupracrustal rocks throughout the complex. All sillimanite is fibrolitic and is confined to the aluminous meta-argillite horizons of the biotite schist. Fibrolite needles are parallel to rock lineation, and sometimes hosted in muscovite, albite, and quartz. There is no textural evidence for the production of sillimanite by a polymorphic phase transition from either kyanite or andalusite. Kyanite was described in previous work by Tabor (1988) at biotite schist localities on the northern shore of the Kabetogama peninsula, near the Rainy Lake Seine-River Fault. Tabor (1988) did not observe the coexistence of kyanite and sillimanite, and did not report textural evidence for the production of kyanite by a phase transition from sillimanite.

Garnet is localized in the aluminous horizons of the biotite schist. Porphyroblasts range from 0.1 to 0.75 mm, and are euhedral to anhedral. Garnets are poikiloblastic with

quartz, plagioclase, muscovite, biotite, and pyrite inclusions. The outer boundaries of subhedral to anhedral garnets are highly irregular. Garnet inclusions record deformation, suggesting crystallization was pre-kinematic to syn-kinematic (Figure 6). The average biotite schist garnet composition is 80% almandine (Table 2).

Amphibole is localized to metavolcanosedimentary horizons, constituting approximately 30% of modal mineralogy. Amphibole is tschermakite, foliated with biotite, and has crystal sizes ranging 0.2 to 0.8 mm.

Accessory phases of zircon, monazite, rutile, apatite, allanite, and epidote occur in the schist. Zircons hosted in biotite are apparent with radiation damage halos. Monazite occurs within the biotite foliation, with some crystals enveloped within biotite laths. These textural relationships suggest monazite crystallization is syn- to post-formation of the metamorphic biotite foliation fabric. Some framwork quartz crystals host small rutile needles. Apatite is elongate with the foliation, with average crystal lengths of 0.1 mm.

4.2 Granitic rocks

Granitic rocks in the VGC include a number of plutonic phases distinguished on the basis of composition, texture, and field relationships (Southwick and Sims, 1979; Day, 1983; Tabor, 1988). Here I describe the Lac La Croix Granite (LLCG) and leucogranite units, both of which are intimately related to the biotite schist as either intrusive or anatectic components. Additionally, on the basis of composition and texture, I describe a distinct new granodiorite unit.

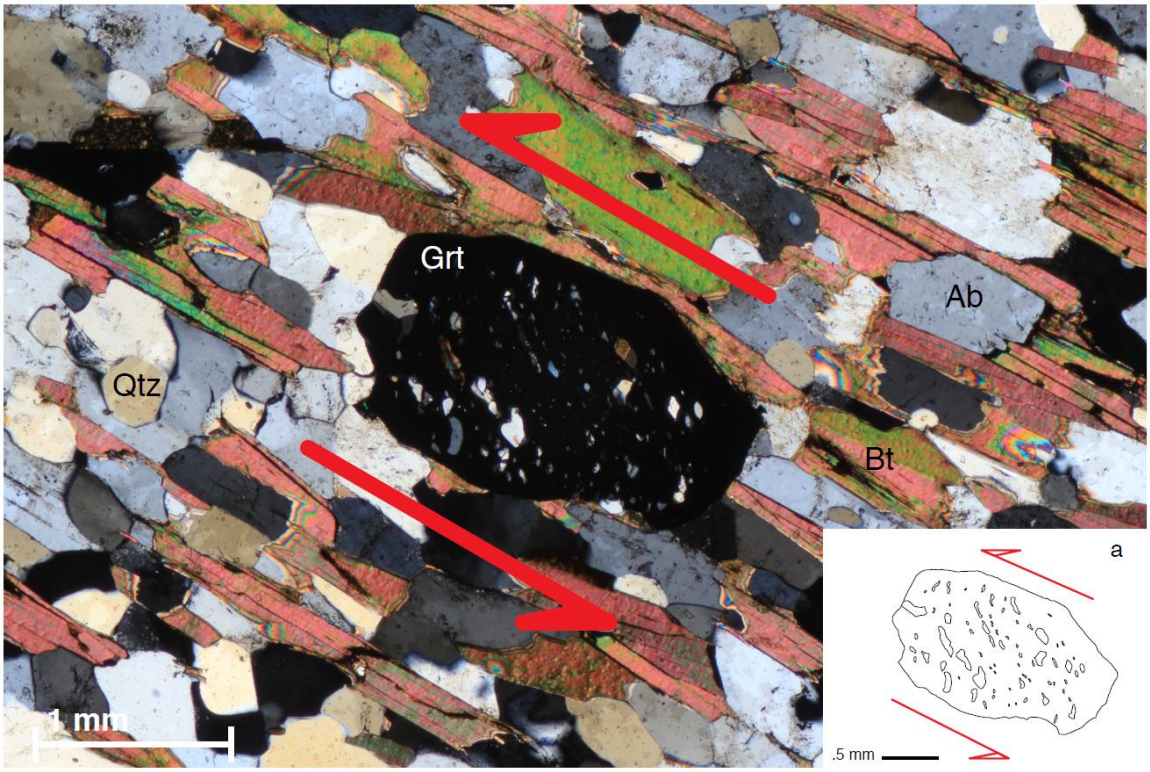

Figure 6. The orientation of poikiloblasts in a garnet is perpendicular to the foliation of the rock. The offset orientation may be result of minor deformation during garnet crystallization. These textures suggest garnet crystallization was pre- to syn-kinematic. Inset (a) highlights the deformation of quartz, albite, and biotite inclusions in the garnet prophyroblast, indicating sinistral rotation.

4.2.1 Lac La Croix Granite

The LLCG is the most abundant granitic phase in the VGC on the basis of surface exposure. A batholith-sized body of the LLCG defines the core of the complex, and grades outwards as granite-schist migmatite into the schistose country rock. Dikes of LLCG intrude the biotite schist in areas proximal to the batholithic core. In outcrop, the granite is pinkish-grey to grey-white in color, and porphyritic with medium to coarse crystal sizes.

The LLCG is a biotite granite (Figure 7). Quartz forms coarse crystals ranging in size from 0.5 mm to 2.0 mm with undulose extinction of quartz indicates a minor degree of solid state, post-crystallization deformation with irregular and sutured intragrain boundaries. Quartz also occurs as inclusions within alkali feldspar phenocrysts. Alkali feldspar is microcline and forms subhedral phenocrysts, with grain sizes of 0.75 to 1.0 mm. Fine-grained examples of alkali feldspar are anhedral, with crystal sizes of 0.25 to 0.35 mm, and are inclusion free. Perthitic exsolution is limited to larger phenocrysts, these exsolution textures suggest early hypersolvus crystallization with exsolution during cooling. Crystallization of smaller microcline grains was subsolvus at lower temperatures during the crystallization of albitic plagioclase feldspar. Plagioclase composition is about An_{25} (determined by the Michel-Lèvy method). Compositional zonation of plagioclase crystals is apparent in the preferential alteration of calcic cores to sericite, whereas sodic rims are thin and unaltered. Advanced alteration of cores results in large laths of irregular muscovite.

Biotite, the primary phyllosilicate phase forms medium-grained laths. Biotite is interstitial between large feldspars and quartz phenocrysts. Chlorite and sericite form concentrated along biotite cleavage planes as alteration products of biotite. Accessory

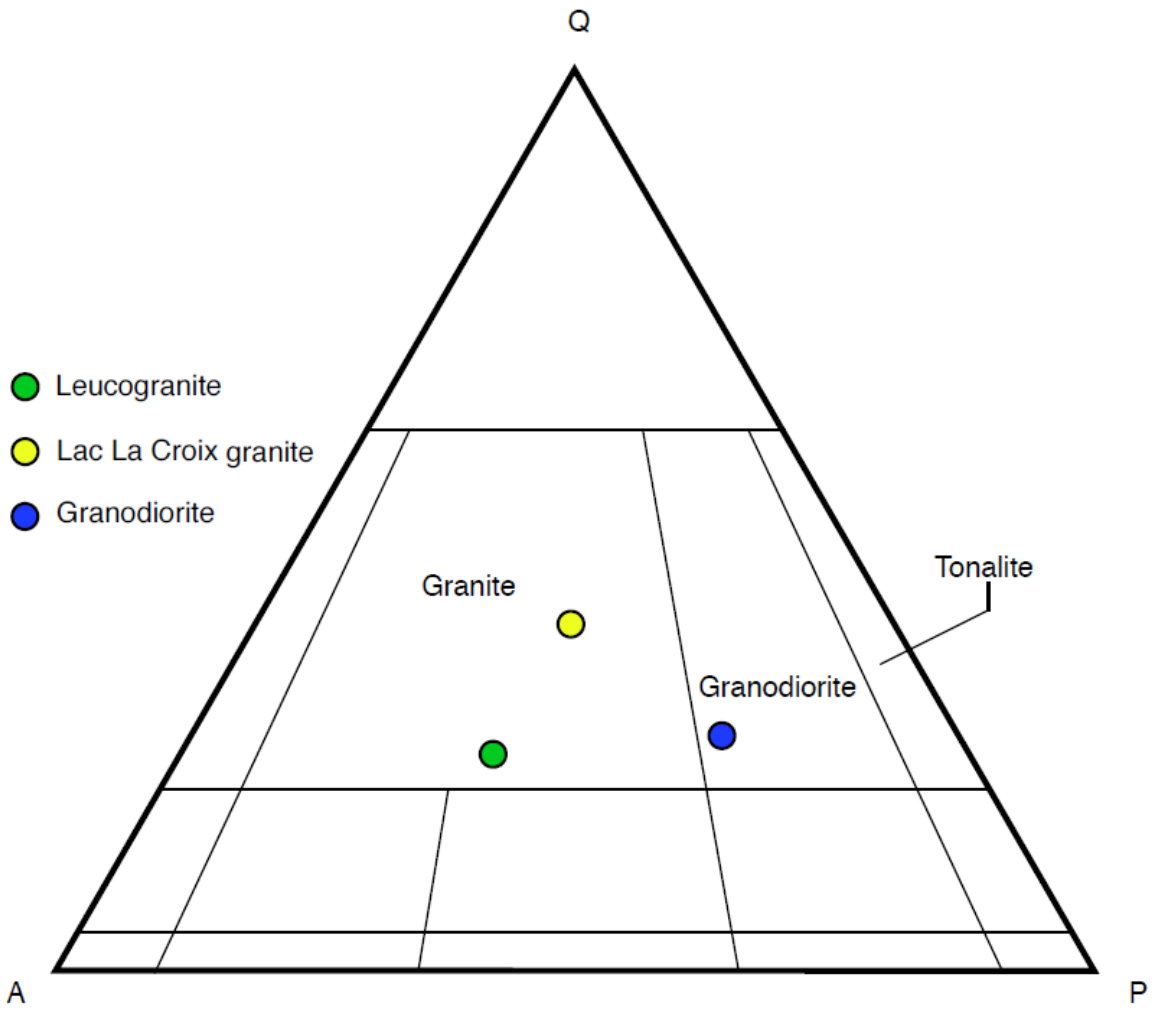

Figure 7. QAP (quartz, alkali feldspar, plagioclase) modal compositions of the Lac La Croix Granite, leucogranite, and granodiorite.

magnetite and biotite as the only primary mica distinguish the LLCG from the leucogranite. Coarse magnetite crystal sizes can be as large as 1 cm.

4.2.2 Granodiorite

Mapping in the study area revealed the presence of a new intrusive rock unit with a granodioritic composition, mineralogically distinct from the granodioritic rocks of the Pelican Lake area noted by Day (1983). I describe this new granodioritic lithology from a locality where granodiorite dikes intrude biotite schist, in an area proximal to a large LLCG body. A grey color and weak biotite foliation distinguish the biotite granodiorite from the LLCG. Compositionally, higher plagioclase abundance distinguishes granodioritic rocks from the LLCG and leucogranite (Figure 7), and crystals are equant and polygonal. Plagioclase is albitic and myrmekitic near grain boundaries with alkali feldspar. Compositional zonation of plagioclase is not apparent. Some plagioclase grains are fully altered to sericite. Undulose extinction and irregular grain boundaries in quartz suggest some degree of post-crystallization deformation. In granodiorite dikes biotite laths define a weak foliation. Melt flow possibly induced the lath shape preferred orientation. Zircon is an accessory phase with crystal sizes of about 0.25 mm. Fe oxides are disseminated throughout the sample and constitute less than 5% of modal mineralogy.

4.2.3 Leucogranite

Leucogranite occurs in dikes, migmatite leucosome, and as large hundred meter scale bodies. Leucogranite dikes cut perpendicular to the foliation of the biotite schist country rock in the northern areas of the complex. Such dikes occur in exposures of biotite

schist on the Kabetogama peninsula. Leucogranite occurs as leucosome in stromatic migmatites. In such examples, leucogranite leucosome forms concordantly with the foliation of the schist melanosome and is commonly isoclinally folded with the foliation.

Leucogranite migmatite also forms rafted structures. In these strucutures large bodies of leucogranite entrain blocks of biotite schist, and blocks are cross-cut by leucogranite dikes. The block hosted dikes predate the emplacement of the leucogranite body. Schist blocks in these systems also appear to have been dissociating into the large body of leucogranite along schist foliation planes. Some intrusive dikes in the schist country rock host pegmatitic muscovite, biotite, and alkali feldspar. Leucogranite is white to white-pink with increasing alkali feldspar concentration.

The leucogranite is a two-mica granite with both primary muscovite and biotite (Figure 7). Quartz is texturally medium to coarse grained with irregular boundaries. Undulose extinction in quartz is ubiquitous. Plagioclase is medium to coarse grained with minor sericite alteration. Coarse plagioclase phenocrysts host quartz inclusions. Alkali feldspar is medium to coarse grained with minor perthitic exsolution. Muscovite occurs both as a primary igneous phase, and in regions of advanced seritization. Primary muscovite form as elongate laths, with size ranging 0.5 to 1.0 mm. Muscovite laths are interstitial between quartz and feldspar phenocrysts. Biotite laths are small relative to muscovite and occur between quartz and feldspar phenocrysts. Biotite alteration to sericite and chlorite is common.

Garnet is subhedral, inclusion free, and distinguishes the leucogranite from the LLCG. Garnet is not a common igneous phase and thus is likely xenocrystic, possibly derived from an adjacent metamorphic lithology. A xenocrystic source is consistent with

the occurrence of other common metamorphic, and likely xenocrystic phases in Quetico leucogranite such as sillimanite and monazite described by Percival and Sullivan (1988) near Lappe, Ontario.

4.3 Migmatite

A number of structural types are used to describe migmatitic rocks (see Mehnert, 1969; Sawyer, 2008). Migmatite is mainly a descriptive term to discuss the structure of a multicomponent lithology containing both metamorphic and igneous elements. In some instances migmatite structural types can be related to a specific mode of migmatization. For example, the felsic leucosome horizons in stromatic migmatites may be the coalesced melt products of anatexis at high metamorphic grade. In cases of rafted migmatites, suspended melanosome blocks and leucosome dikes are commonly interpreted as the result of melt injects from an external source.

This relation of migmatite structure to migmatization mode should be cautious as metamorphic systems are complex. Large volumes of anatectic melt can easily entrain melanosome blocks, forming rafted migmatites. Leucosomal stroma can also be product of melt injections along preexisting weak foliation planes. Thus, migmatite structural type alone is an inconclusive petrogenetic indicator. However, when these structural observations are paired with metamorphic P-T estimates and geochronology, genetic models are strengthened.

There are a wide variety of migmatites in the VGC which are possible evidence of both injection and partial melting (Figure 8). The ratio of leucosome to melanosome in migmatite varies regionally. Migmatite proximal to the core of the complex incorporates a

Figure 8. Field photographs of representative migmatite types. (a) Block of schist rafted in leucogranite leucosome, in which schist blocks are digested in the leucosome, dissociating along foliation planes. (b) Leucogranite dike cross-cutting biotite schist. (c) Schist-rich migmatite with cross-cutting leucogranite leucosome exhibiting both stromatic and veining structures. (d) Stromatic schist-rich migmatite with leucogranite leucosome, leucosome is forming concordantly with the foliation. (e) Schist-rich migmatite with LLCG neosome, veined-to-rafted structure. (f) Stromatic-to-rafted schist migmatite, with boudinaged LLCG leucosome.

greater amount of granitic leucosome, while leucosome abundance is lower in migmatites on the margins of the VGC. To simplify the diverse assemblage of migmatite types, I describe migmatites primarily by leucosome lithology.

4.3.1 Leucogranite-schist migmatite

Within the biotite schist, leucogranite dikes cut perpendicular to the foliation of the rock and indicate leucogranite emplacement was late relative to the age of the biotite schist. More proximal to the core of the complex, high densities of dikes migmatize the biotite schist with leucogranite leucosome. Bands of leucogranite concordant with country rock foliation form stromatic leucogranite-schist migmatites. In stromatic structures, leucosome is isoclinally folded with the foliation of the rock, suggesting migmatization was pre-kinematic to syn-kinematic. Voluminous leucosomal stroma host nebulous textures of dissociating schist melanosome. In some examples, leucosome stroma are connected to leucogranite dikes, suggesting dikes may have acted as melt conduit filling stroma.

In rafted leucogranite-schist migmatites large bodies of leucogranite envelope blocks of biotite schist melanosome. Schist melanosome blocks host leucogranitic dikes and some blocks have been stromatically migmatized with leucogranite. Leucogranite dikes and stroma texturally predate the rafting of blocks. This may indicate initial migmatization emplaced dikes and stromatic leucosome. As migmatization advanced, larger volumes of leucogranite melt rafted and dissociated the migmatized biotite schist country rock.

4.3.2 LLCG-Schist migmatite

LLCG-schist migmatite occurs on the margins of the granitic core of the complex. Rafted and block type migmatite is associated with a high density of LLCG dikes in biotite schist. LLCG leucosome stroma are folded and boudinaged with the foliation of the biotite schist suggesting leucosome emplacement was pre- to syn-kinematic. Swarms of LLCG dikes in country rock form veining migmatites. In some cases, stromatic migmatite is cross-cut by later stages of LLCG dikes.

5 Metamorphism

5.1 Metamorphic reactions and textures

First order constraints on biotite schist metamorphic P-T conditions come from thin section observations of reaction textures and phase equilibria. The metamorphic assemblage in the biotite schist is biotite + albite + quartz ± muscovite ± garnet ± sillimanite ± potassium feldspar. The spatial distribution of these metamorphic assemblages is variable and correlates to the heterogeneous bulk rock composition of the sedimentary protolith. In addition to biotite + albite + quartz, two distinct peak assemblages, (a) and (b) occur.

a. muscovite + albite + potassium feldspar

b. muscovite + albite + sillimanite

Assemblage (b) characterizes schist exposed at a road cut in the southern region of the VGC, north of Orr, MN. There, sillimanite as fibrolite constitutes 20% of modal mineralogy. Sillimanite partially replaces M1a muscovite and is parallel with rock lineation. M1b muscovite is porphyroblastic and symplectically intergrown with quartz and albite. M1a muscovite is more paragonitic relative to M1b muscovite, with representative K/Na values of 7.3 and 10.7, respectively (determined with EDS analyses). The sample hosting assemblage (b) does not contain potassium feldspar. Textures and phase equilibria indicate assemblage (b) to be the result of reaction (1).

(1) Na-rich muscovite + quartz = sillimanite + albite + K-rich muscovite + H_2O

Figure 5b is a micrograph of the textures and equilibria associated with reaction (1).

Assemblage (a) is noted in a sample collected in the northern VGC from the northern shore of Lake Kabetogama. Muscovite as euhedral laths of 0.75 mm shows no preferred orientation and is the only discernable muscovite generation. Symplectic quartz and albite intergrowths with muscovite are common. Porphyroblastic potassium feldspar is microcline and poikiloblastic with inclusions of muscovite, biotite, quartz, and albite. Porphyroblasts size is 1.0 mm to 1.25 mm, and crystals are anhedreal with irregular boundaries. The sample hosting this assemblage does not contain aluminosilicate. The photomicrograph in Figure 5a is of the equilibria and textures associated with this assemblage.

The stability of these phases can be explained at the conditions associated with the tie-line arrangements derived by Evans and Guidotti (1966), shown in Figure 9. Their work addresses the equilibria of phases associated with the reaction of muscovite breakdown by reaction (2).

(2) muscovite + quartz = potassium feldspar + sillimanite + H_2O

Evans and Guidotti (1966) show reaction (2) to be the summation of a number of continuous reactions over a range of 600 – 650 °C. The tie-line arrangement in Figure 9 describes the stability of phases at conditions of muscovite stability (i.e., below muscovite breakdown). Their work predicts muscovite instability over a wider range of bulk compositions at temperatures higher than those associated with the equilibria projected in

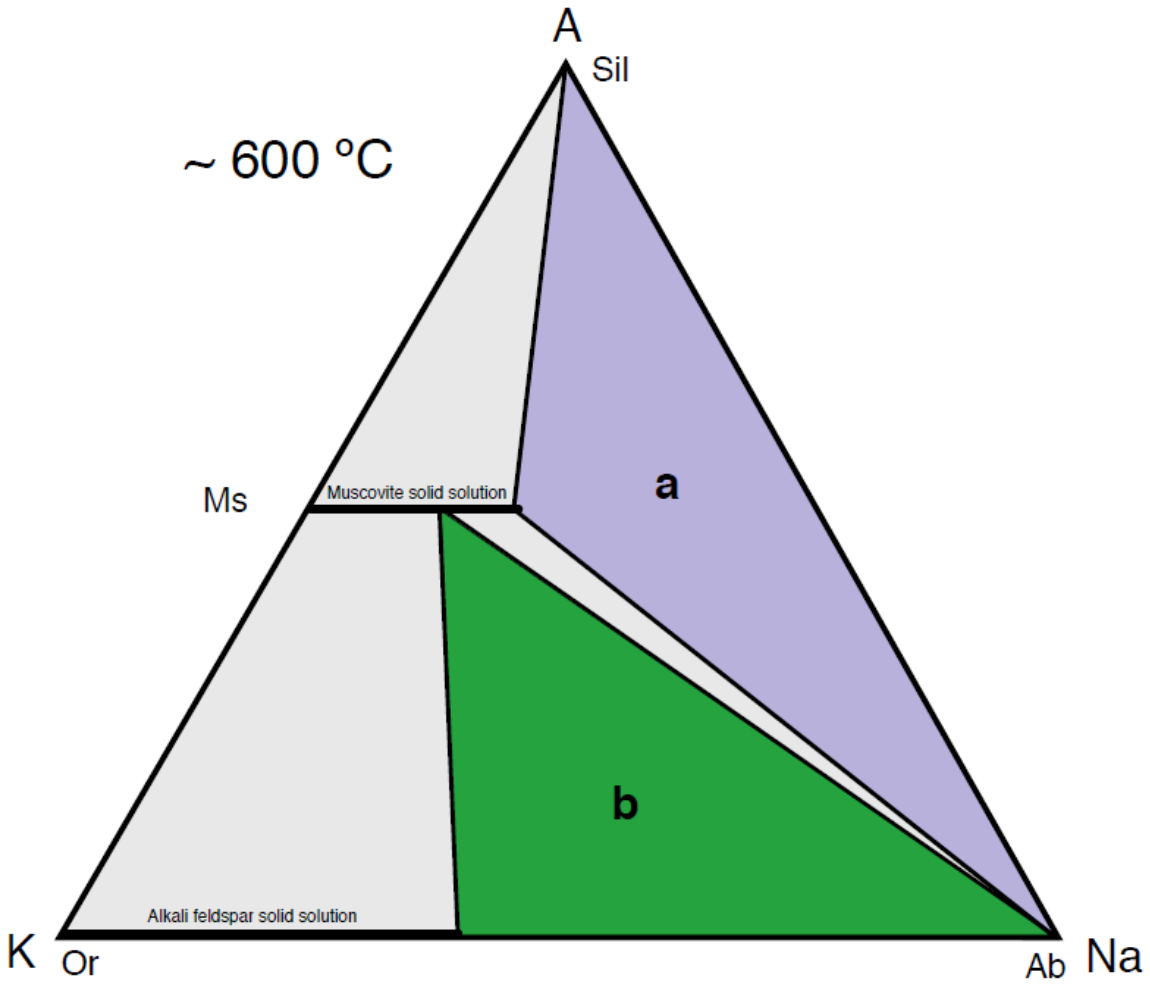

Figure 9. Stable assemblages of the biotite schist units in AKNa space, at a temperature of ~ 600 °C, below the muscovite breakdown as defined by Evans and Guidotti (1966). Parageneses representative of assemblages (a) and (b) indicated.

Figure 9. The widespread stability of muscovite and textural evidence for reaction (1) indicate that peak P-T did not exceed ~ 650 °C.

5.2 Garnet compositional profiles

Garnets in metamorphic rocks are commonly compositionally zoned. Compositional zonation implies a lack of local equilibrium and must be considered when conducting spot chemical analysis to calculate temperatures by garnet-biotite Fe-Mg ion-exchange. Profiles of garnet porphyroblasts in biotite schist show little zonation. Garnet composition averages 80% almandine and 17% spessartine, and varying trace amounts of grossular and pyrope components (Figure 10).

5.3 Garnet-biotite thermometry

The Fe-Mg ion-exchange thermometer was applied to garnet-biotite assemblages in biotite schist at five localities in the VGC. Temperatures were derived using the Ferry and Spear (1978) calibration of Fe-Mg partitioning between annite and almandine phases. Temperatures are calculated with the garnets in biotite schist at five localities in the complex. The oxide and cation values reported in Table 2 and Table 3 are the average values of five point analyses on each grain. The A and B columns for a single sample report data from two garnet-biotite pairs analyzed in the same sample. The samples chosen form geographically diverse set across the VGC to explore a possible metamorphic temperature gradients in the complex. The calculated temperatures range between 420-620 ˚C (Figure 11).

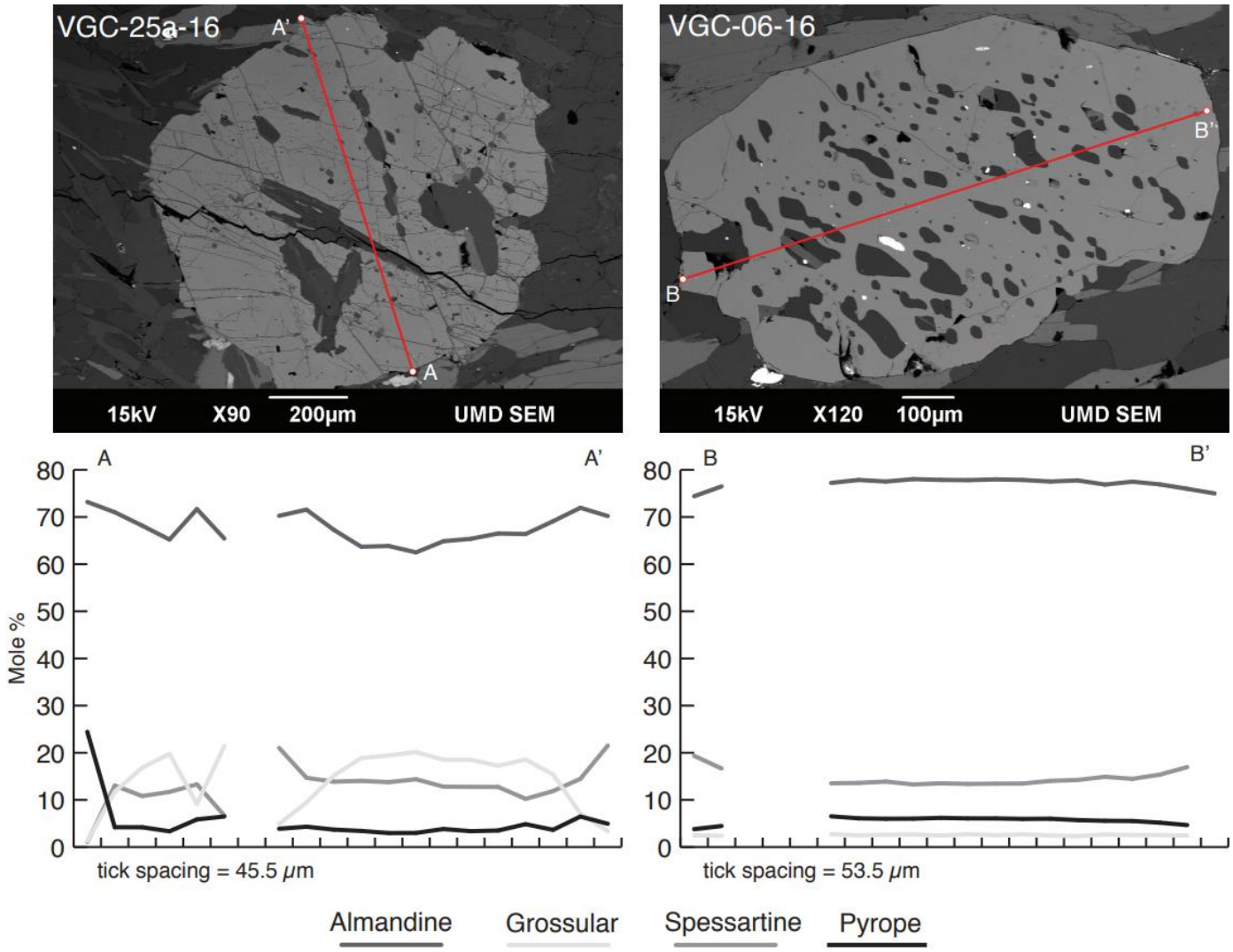

Figure 10. Representative compositional profiles for garnets in the biotite schist. Each profile consists of 20 EDS spot analyses.

Table 2. Average garnet compositions at five localities of biotite schist. A and B columns report compositions of two garnets at the same locality. The reported compositions for each garnet are the average of five WDS spot analyses.

Sample No:	VGC-06-16		VGC-31-16		VGC-40-16	VGC-25a-16	VGC-37-16	
	A	B	A	B			A	B
Oxide wt %								
SiO_2	36.50	36.75	36.61	36.69	36.83	36.48	36.26	37.48
TiO_2	0.02	0.00	0.12	0.03	0.01	0.33	0.06	0.07
Al_2O_3	21.29	20.50	20.62	20.63	20.59	20.26	20.68	20.75
Cr_2O_3	0.02	0.04	0.00	0.01	0.01	0.03	0.04	0.05
FeO	31.92	32.95	32.04	32.25	26.86	30.39	28.56	28.05
MnO	6.44	6.06	8.17	8.32	11.77	6.59	5.99	4.89
MgO	2.42	2.61	1.71	1.62	2.03	1.96	2.66	2.56
CaO	1.09	1.12	1.11	1.12	1.59	3.43	4.71	6.29
TOTAL	99.69	100.02	100.39	100.66	99.68	99.48	98.97	100.15
Cations, based on 12 O								
Si	2.967	2.989	2.982	2.984	3.002	2.980	2.956	2.999
Ti	0.001	0.000	0.007	0.002	0.001	0.021	0.003	0.004
Al	2.039	1.965	1.980	1.977	1.977	1.951	1.987	1.957
Cr	0.001	0.002	0.000	0.001	0.000	0.002	0.003	0.003
Fe	2.171	2.241	2.183	2.194	1.830	2.076	1.947	1.877
Mn	0.444	0.418	0.564	0.573	0.812	0.456	0.414	0.332
Mg	0.293	0.316	0.207	0.196	0.246	0.239	0.323	0.306
Ca	0.095	0.098	0.097	0.097	0.139	0.300	0.411	0.539
TOTAL	8.012	8.028	8.020	8.025	8.008	8.023	8.045	8.017

Table 3. Average biotite compositions at five localities of biotite schist. A and B columns report compositions of two biotites at the same locality. The reported compositions for each biotite are the average of five WDS spot analyses.

Sample No:	VGC-06-16		VGC-31-16		VGC-40-16	VGC-25a-16	VGC-37-16	
	A	B	A	B			A	B
Oxide wt %								
SiO_2	34.84	35.79	36.13	34.90	35.84	35.62	35.77	36.07
TiO_2	1.84	1.87	1.61	1.43	1.11	1.78	2.04	1.73
Al_2O_3	20.36	20.23	19.90	20.00	19.16	19.45	18.26	18.02
Cr_2O_3	0.07	0.12	0.04	0.03	0.07	0.08	0.14	0.09
FeO	19.84	19.89	20.26	20.85	19.81	20.36	19.19	18.71
MnO	0.13	0.14	0.14	0.17	0.33	0.18	0.21	0.17
MgO	9.54	9.78	9.36	10.14	10.26	9.29	10.57	11.02
CaO	0.00	0.00	0.01	0.02	0.02	0.01	0.02	0.05
Na_2O	0.28	0.26	0.30	0.19	0.14	0.18	0.14	0.23
K_2O	9.24	9.19	9.64	8.56	9.81	9.72	9.46	9.12
TOTAL	96.14	97.27	97.40	96.29	96.56	96.68	95.81	95.20
Cations, based on 22 O								
Si	5.264	5.330	5.393	5.269	5.405	5.374	5.418	5.472
Ti	0.209	0.209	0.181	0.162	0.125	0.203	0.233	0.198
Al	3.625	3.550	3.501	3.560	3.406	3.459	3.259	3.223
Cr	0.008	0.014	0.005	0.004	0.009	0.009	0.017	0.010
Fe	2.507	2.477	2.529	2.633	2.498	2.569	2.431	2.373
Mn	0.016	0.018	0.018	0.022	0.042	0.023	0.026	0.022
Mg	2.149	2.170	2.083	2.281	2.307	2.090	2.387	2.492
Ca	0.001	0.001	0.002	0.004	0.004	0.001	0.003	0.008
Na	0.082	0.074	0.086	0.056	0.042	0.054	0.041	0.067
K	1.780	1.746	1.835	1.648	1.887	1.871	1.829	1.764
TOTAL	15.642	15.588	15.633	15.639	15.727	15.652	15.646	15.630

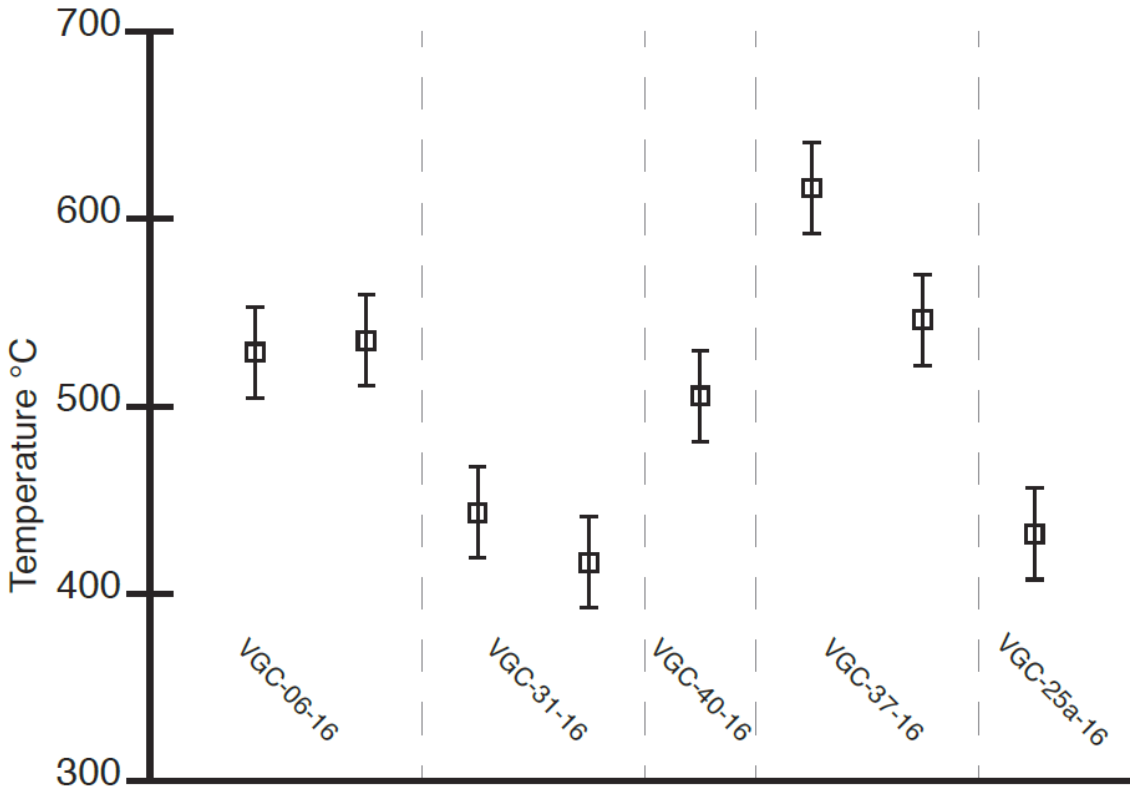

Figure 11. Garnet-biotite temperatures in samples of VGC biotite schist using standard calibration of Ferry and Spear (1978). Uncertainties of ± 50 ˚C on each point correspond to ± 0.01 error in almandine, pyrope, phlogopite, and annite mole fractions.

5.4 Estimates of biotite schist peak P-T

Although the reactions and phases associated with muscovite breakdown by reaction (2) at approximately 650 ˚C are apparent, the reaction products of coexisting of potassium feldspar and sillimanite are absent in all samples. Rather, good textural evidence for reaction (1) and the phase equilibria favor metamorphism approaching, but not exceeding the conditions associated with reaction (2). Thus, petrographic evidence suggests peak temperature between 600 ˚C and 650 ˚C. Garnet-biotite thermometry records the temperatures of metamorphism between 420 and 620 ˚C. The upper limits of this range are consistent with the textural evidence for peak metamorphism in the middle amphibolite facies, between 4-5 kbar. Importantly, these calculations show metamorphic conditions approached, but failed to exceed the limit associated with complete muscovite dehydration and partial melting. Thus, the peak P-T estimates for biotite schist metamorphism restrict the potential for partial melting as the source of granitic rock in the VGC.

6 Geochronology

Zircon and monazite U-Pb geochronology was used to establish a temporal relationship between biotite schist metamorphism and granitic crystallizations. Ages were determined by *in situ* LA-ICPMS analyses. The zircon ages of biotite schist record an inherited detrital history, whereas monazite ages from the schist constrain the timing of metamorphism. Zircon ages of the LLCG, leucogranite, and granodiorite units record the crystallization age of these bodies. Isotopic data were processed in Isoplot (Ludwig, 1999).

Zircon and monazite isotopic data are displayed graphically in Figure 13, Figure 15, and Figure 17, plotted with 1σ uncertainty. Isotopic data is reported for biotite schist zircons in Appendix D, biotite schist monazite in Appendix E, and granitic zircon in Appendix F.

6.1 Biotite schist zircon

The zircon ages of metasedimentary rocks often provide both the age of metamorphism and the inherited age of sediment provenance. Metamorphic zircon growth is accommodated at the amphibolite facies and higher grades (Hoskin and Schaltegger, 2003). Commonly under these conditions, inherited detrital zircon grains nucleate new zircon crystallization as rim overgrowths. Thus, zircon growth under metamorphic conditions results in crystals with complex internal zonation.

Cathodoluminescence (CL) imagery is the principal tool used to explore the internal morphology and structure of zircon crystals. CL emission is governed by transition element (TE) and rare-earth element (REE) composition (Corfu et al, 2003). The structure and arrangement of zones in single zircon crystals is clearly visible in CL emission imaging, as

the TE and REE composition between zones varies. Biotite schist zircons host oscillatory zonations, common features of magmatic and high temperature metamorphic zircon growth. These growth structures define two or more unconformable, but semi-concentric domains within single schist zircons (Figure 12). Thin homogenous mantles with medium to bright CL emission characterize the rims of some crystals. Mapping of these complexities with CL imaging guided *in situ* laser analyses to explore the age of the multiple growth domains within single crystals.

The analysis of interior oscillatory zones within single grains produced reliable concordant to near-concordant U-Pb ages. As metamorphism peaked in the middle amphibole facies, temperatures were likely to have been too low to generate the domains with oscillatory zonations. These oscillatory zones are therefore interpreted as magmatic in origin and detrital, having crystallized in the melt of the plutonic source. Oscillatory overgrowth on oscillatory cores may reflect short-interval episodic overgrowth crystallization in a dynamic magmatic environment.

The thin outer mantles on schist zircons commonly yielded discordant U-Pb analyses with large errors. In many cases, the analytical beam diameter exceeded the width of the overgrowth mantles and multidomainal analyses resulted. On the basis of morphology and CL emission, these thin features are interpreted to be the result of metamorphic overgrowth. No reliable ages are determined for these overgrowth domains in light of the analytical limitations and grain complexities. Therefore, zircons in the biotite schist are detrital, and the ages reported here accurately constrain the ages of sources in sediment provenance.

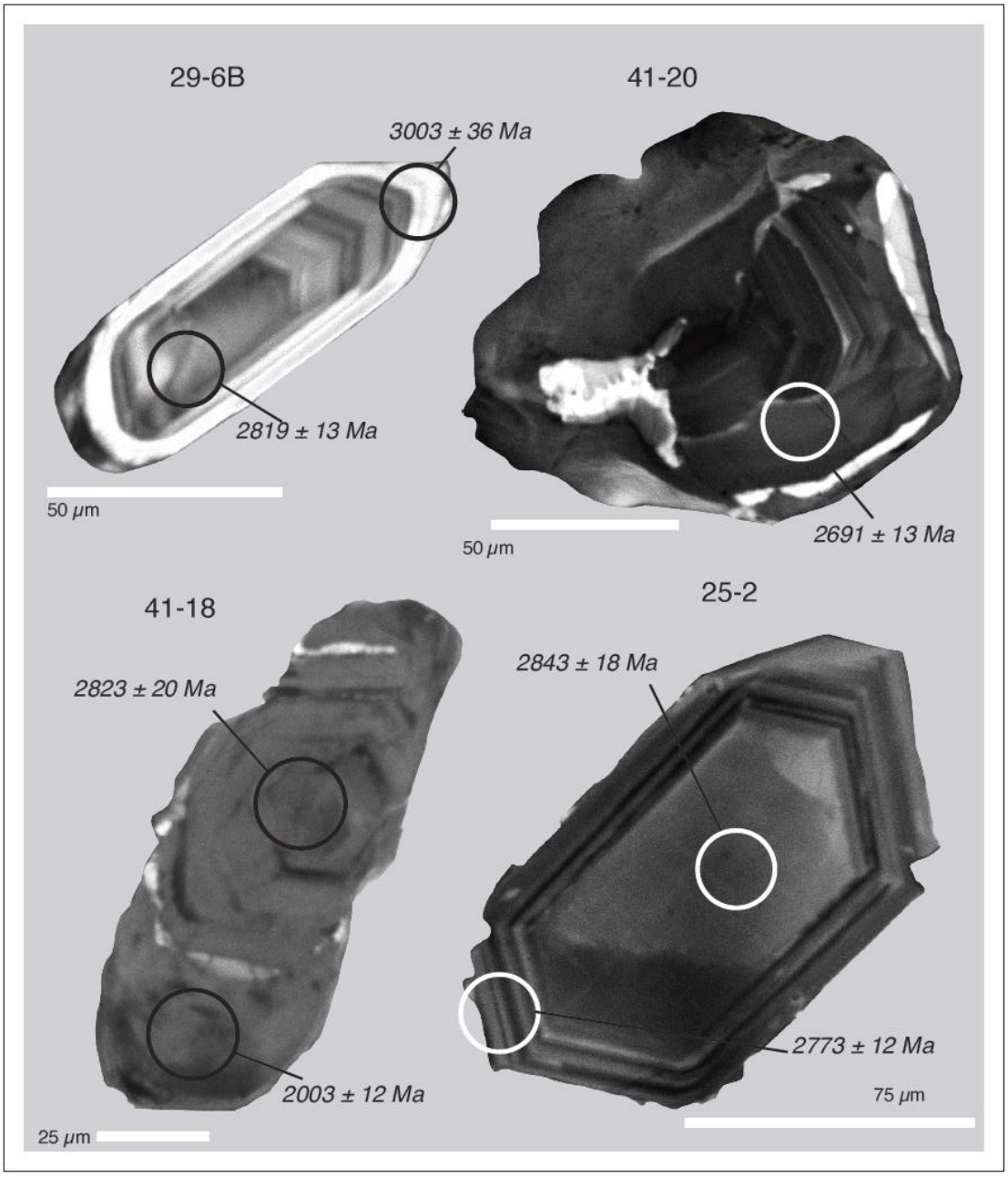

Figure 12. Cathodoluminescence (CL) images of biotite schist detrital zircons. Oscillatory structure characterizes the cores of grains, indicative of crystallization in a magmatic system or at high metamorphic temperatures. Thin, bright rim overgrowths are likely metamorphic. No reliable ages were determined for metamorphic overgrowth domains. The youngest confident detrital zircon analysis is the age of grain 41-20.

6.1.2 Sample VGC-25-16

Sample VGC-25-16 is a biotite schist from the northern margin of the VGC where the country rock is unmigmatized. On a Wetherill plot these age data show a significant degree of discordance. The discordant analyses are systematically shifted down and off the concordia curve as lead isotope concentrations are systemically lower. Such discordance is likely due to common Pb-loss induced during the metamorphism of the biotite schist. Concordant analyses cluster at ages of about 3100, 2900, and 2750 Ma (Figure 13a). Discordant analyses interpolate a Pb-loss trajectory that regresses an upper intercept age at 2725 ± 14 Ma. The $^{207}Pb/^{206}Pb$ ages of grains with less than 10% discordance have population age groupings at 3250, 3100, 2950, and 2710 Ma (Figure 13b). The main source of sediment provenance is represented by an age population of about 2710 Ma.

6.2.2 Sample VGC-29-16

Sample VGC-29-16 is a biotite schist migmatized with stromatic leucogranite leucosome on the southern shore of the Kabetogama peninsula. Discordance on a Wetherill diagram follows a regular Pb-loss trajectory likely induced during metamorphism, and regresses an upper intercept age at 2721 ± 10 Ma. Analyses with less than 10% discordance cluster on concordia between 2700 and 2800 Ma (Figure 13c). The $^{207}Pb/^{206}Pb$ age distribution is unimodal for analyses with less than 10% discordance, with a peak age frequency at about 2715 Ma (Figure 13d).

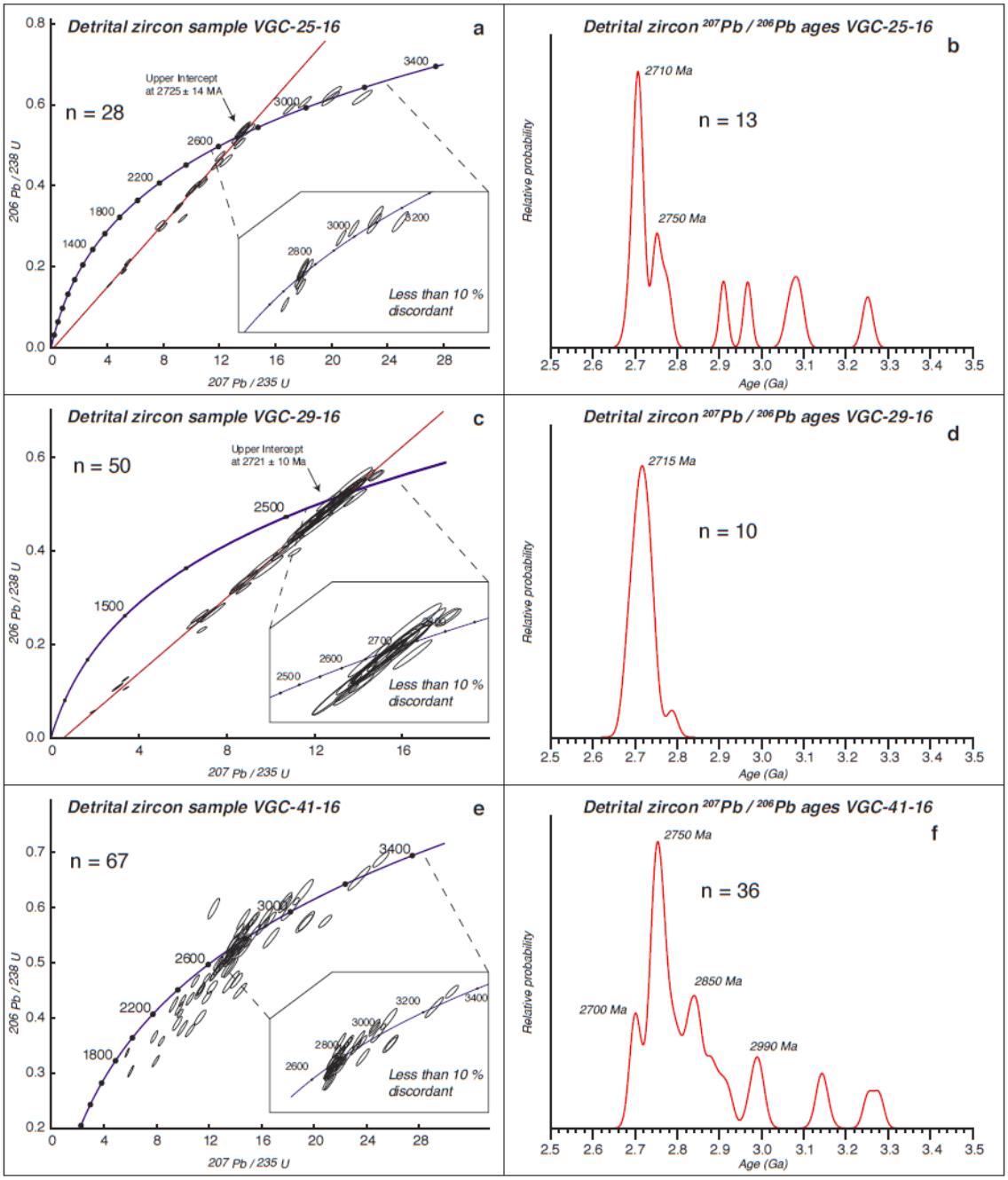

Figure 13. Concordia diagrams with zircon U-Pb data at three localities of biotite schist. Insets in concordia plots highlight more accurate data with less than 10 % discordance. Probability distributions of $^{207}Pb/^{206}Pb$ ages for the less than 10 % discordant data are plotted to the right of the concordia diagrams. $^{207}Pb/^{206}Pb$ probability distributions are annotated with age peaks.

6.2.3 Sample VGC-41-16:

This sample of biotite schist melanosome was collected from a strongly migmatized locality in the central VGC. Concordant analyses on a Wetherill diagram plot near 2700 Ma and older. Discordance is both positive and negative, and appears to follow multiple Pb-loss trajectories, which regress to multiple upper intercept ages (Figure 13e). A number of sediment provenance ages are apparent in the multimodal distribution of zircon $^{207}Pb/^{206}Pb$ ages from analyses with less than 10% discordance. Peak age groupings are at about 3250, 2850, 2750, and 2700 Ma (Figure 13f). A small population with an age peak of about 2690 Ma represents the youngest detrital component observed in the biotite schist, with the youngest concordant zircon analysis having a $^{207}Pb/^{206}Pb$ age of 2690 ± 12 Ma (see CL image of youngest grain, 41-2, Figure 12).

6.3 Biotite schist monazite

Monazite geochronology is a useful tool for the investigation of many metamorphic petrochronological problems. Monazite U-Th-Pb ages can be used to determine the timing of prograde to peak metamorphic P-T paths (Kohn, 2016). *In situ* LA-ICPMS allowed for monazite laser spot analyses on grains in thin sections. Textural geochronology indicates that monazite crystallized during or after development of the metamorphic biotite foliation, as crystals are within or intergrown with biotite laths.

Polyphase metamorphism can result in multiple growth domains within a single monazite crystal. These domains are evident in REE and TE zonation. I mapped Y, Ce, La and Th concentrations in monazite grains to guide *in situ* laser analyses towards homogenous domains and explore the possibility of polyphase metamorphic history. In the

monazites studied no grains display significate zonation or heterogeneity (Figure 14). This indicates monazite crystallization in the biotite schist is likely the product of a single metamorphic phase.

6.3.1 Sample VGC-10-16

Monazite in this sample is hosted within the foliation of biotite schist melanosome. This locality is migmatized with LLCG, leucogranite, and granodiorite leucosomal phases. On a Wetherill diagram nine analyses follow a well-defined Pb-loss trajectory. The upper intercept of this trajectory is 2671 ± 24 Ma (Figure 15a). The best estimate for the age of monazite growth in this sample is a weighted-mean of the $^{207}Pb/^{206}Pb$ ages, at 2670 ± 11 Ma (Figure 15b).

6.3.2 Sample VGC-34-16

Monazite in this sample is hosted within biotite schist foliation from a locality on the southern shore of the Kabetogama peninsula. The biotite schist county rock hosts small leucogranite dikes of ~ 10 cm width, locally intruded perpendicular to foliation. Of the four analyses on three grains, two are discordant. The concordia age of the most concordant analysis is 2684 ± 12 Ma (Figure 15c). The oldest analysis in Wetherill space, though concordant, has the largest error and therefore is unreliable. The weighted-mean of the $^{207}Pb/^{206}Pb$ ages of the two most concordant analyses is 2728 ± 27 Ma (Figure 15d). The best estimate for the timing of monazite crystallization at this locality is given by the concordia age of the single most concordat analysis, at 2684 ± 12 Ma.

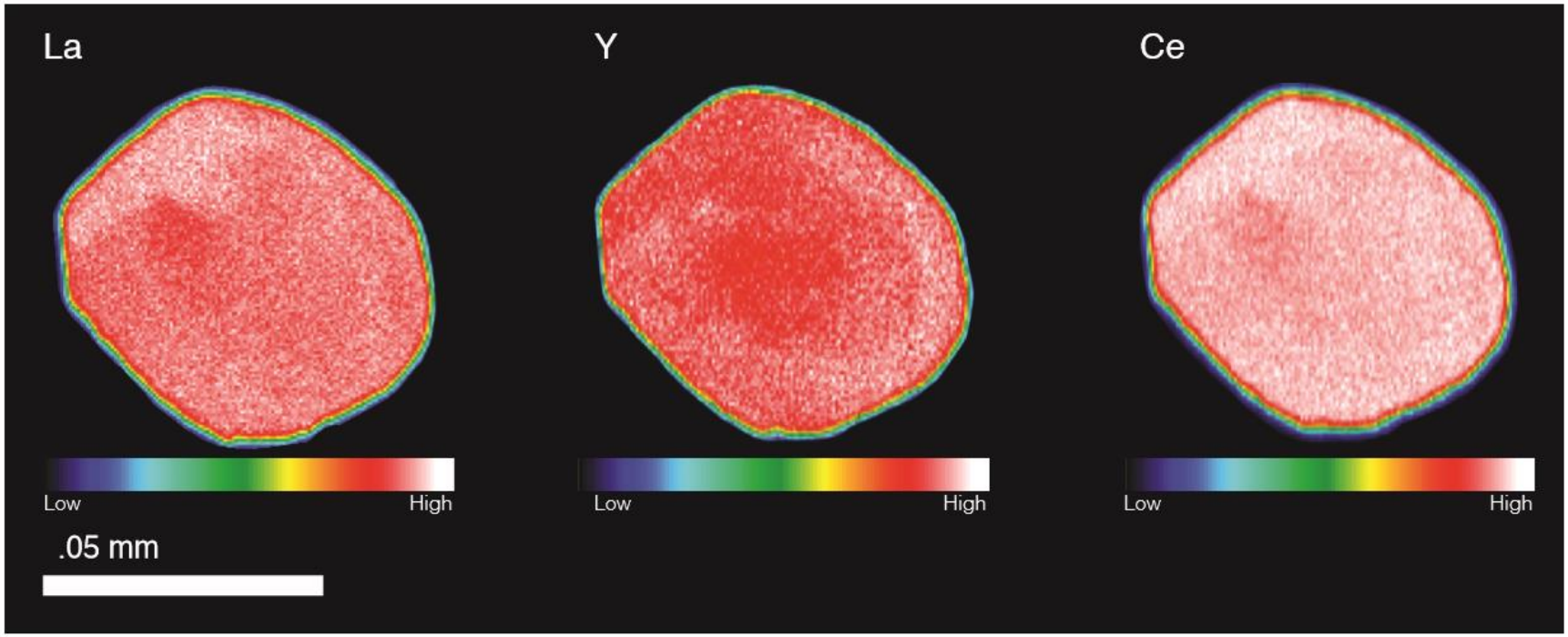

Figure 14. La, Y, and Ce compositional maps of monazite in biotite schist. Note a lack of zonation defined by REE composition consistent with crystallization during a single metamorphic event. The lower compositional values near grain rims are an analytical edge effect and do not reflect actual lower values. This example monazite is from sample VGC-10-16.

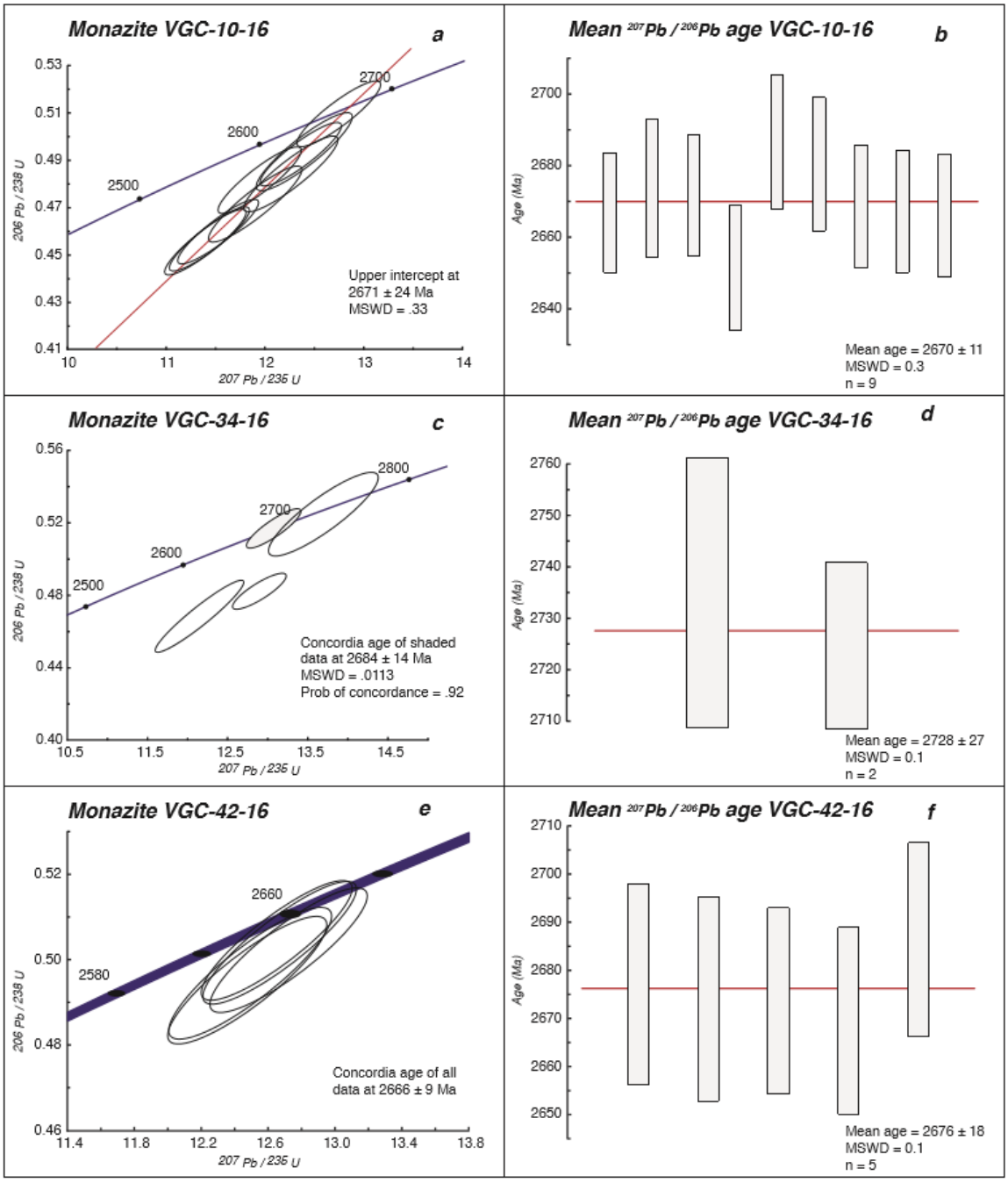

Figure 15. U-Pb concordia diagrams and weighted-mean $^{207}Pb/^{206}Pb$ ages of monazite in biotite schist. The best estimate for the age of monazite crystallization in the biotite schist is given by the weighted mean ages of monazite in samples VGC-10-16 and VGC-42-16, at ~ 2675 Ma.

6.3.3 Sample VGC-42-16

This sample is representative of biotite schist melanosome from a migmatized locality hosting LLCG as leucosome. Five near-concordant analyses provide a concordia age of 2666 ± 9 Ma (Figure 15e). A weighted-mean $^{207}Pb/^{206}Pb$ age of these analyses is 2676 ± 18 Ma (Figure 15f) and is considered the best estimate for the age of monazite growth in this sample.

6.4 Granitic zircon

Zircon U-Pb ages were determined for the three distinct granitic lithologies recognized in the field. Zircons from these samples show oscillatory magmatic zonation (Figure 16). Some crystals host a second oscillatory magmatic overgrowth, akin to the morphology of the biotite schist zircons detrital cores. Figure 17 plots the data of all analyses made. Only those with near-concordant results or which show normal Pb-loss behavior are used to regress intercept ages (ellipses shaded grey). Despite individual grain complexity and discordance by Pb-loss, the U-Pb data provide geologically reasonable constraints for the crystallization age of these igneous units.

6.4.1 Leucogranite, VGC-23-16

This sample was collected from a leucogranite body which hosts rafted blocks of migmatized biotite schist. Zircons have oscillatory zonal structures, with some examples preserving two distinct oscillatory domains (as seen in grain 23-4 Figure 16). Fifteen analyses show a strong degree of discordance on a Wetherill plot. Eight analyses (shaded in grey) regress a Pb-loss concordia intercept age at 2708 ± 94 Ma. Large error in the age

Figure 16. CL images of zircons from the major plutonic units in the VGC. Complex U-Pb data in Wetherill space may be related to the multiple magmatic domains within single crystals, notable in grains 44-12 and 48-2.

of this intercept may be evidence of a Pb-loss event shortly after crystallization, causing some analyses to be systematically shifted along the concordia to a younger apparent age.

6.4.2 Lac La Croix granite, VGC-44-16

This sample represents the granitic rock in the batholithic LLCG core of the complex. Zircons are oscillatory zoned, with some preserving two distinct zones of oscillatory structure. On a Wetherill plot, 17 analyses show a strong degree of discordance (Figure 17). Twelve analyses (shaded in grey) regress a Pb-loss trajectory to an upper intercept age at 2673 ± 63 Ma. The most concordant U-Pb analysis has a $^{207}Pb/^{206}Pb$ age of 2668 ± 10 Ma, and is the best estimate for the crystallization age of the LLCG.

6.4.3 Granodiorite, VGC-48-16

This sample was collected from a dike exposed in a road cut 0.2 km south of the monazite dated sample VGC-10-16. Zircons show both sector and oscillatory zoning, with some preserving two distinct zones of oscillatory structure (as seen in grain 48-2, Figure 16). Twelve of the 14 analyses (shaded in grey) regress and intercept along a Pb-loss trajectory to 2684 ± 23 Ma, and is the best estimate for the age of crystallization (Figure 17).

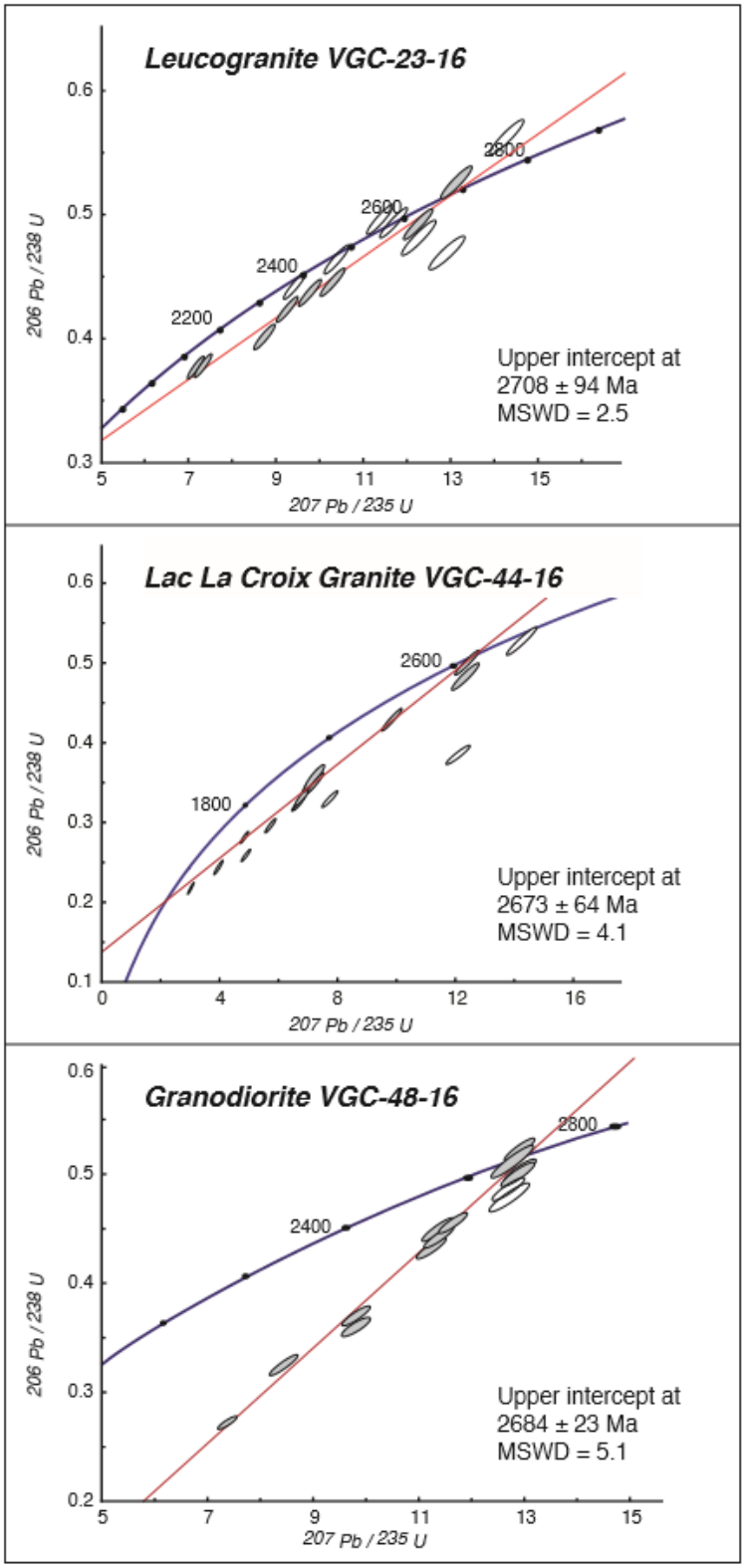

Figure 17. U-Pb concordia plots diagrams and upper-intercept ages for the major plutonic units in the VGC

7 Discussion

7.1 Constraints on metagreywacke protolith provenance

The quartzofeldspathic mineralogy of the biotite schist suggests protolith sediments were greywacke. The abundance of plagioclase in the assemblage indicates sediments were weathered from a magmatic source. A significant modal quartz component may further imply the magmatic source was felsic, and possibly a compositionally evolved plutonic rock.

Albite in the biotite schist is largely detrital, having crystallized in a magmatic system, and it retains an angular morphology and polysynthetic twins after deposition and metamorphism. Detrital zircons are elongate and prismatic. The internal structure of these zircons is oscillatory and likely the product of growth in a magmatic system. Therefore, these elongate zircons have endured sedimentary transport from a magmatic source to deposition in the greywacke protolith. Given that detrital zircons remain elongate, transport in the sedimentary system caused minimal grain abrasion and, thus, was possibly over a short distance. Conversely, mature and well-rounded detrital grains would be suggestive of longer distances of sediment transport, from more distal sources. In the case of short transport distances, the source of protolith sediments may have been proximal to the depositional basin.

Based on inferred short sediment transport distances, the detrital age population is representative of a provenance proximal to the depositional basin. The geologic evolution of the provenance region is represented by prominent age peaks at 2850, 2750, 2715, 2710, and 2700 Ma. These frequent ages likely represent significant sediment contributions from either individual felsic plutonic bodies or magmatic pulses in the source area. The

distribution of these ages records the evolution of the local and proximal source region to be characterized by five major felsic plutonic crystallization or magmatic pulses during the ~ 150 Ma prior to biotite schist metamorphism. Relatively less sediment contribution is noted from older, possibly more distal, ~ 2900 and ~ 3250 Ma sources.

The $^{207}Pb/^{206}Pb$ age of the youngest reliable detrital zircon analysis constrains the maximum age of protolith deposition to be 2690 ± 12 Ma. This age of deposition in the VGC is consistent with that in other areas of the Quetico belt to the east. Percival and Sullivan (1988) constrained the lower age limit of protolith deposition at 2702 ± 4 Ma, in sampling near Lappe, Ontario. Davis et al. (1990) reported the maximum age of protolith deposition at 2698 ± 3 Ma, in sampling near Atikokan, Ontario.

7.2 Grade and timing of biotite schist metamorphism

Quantitative garnet-biotite thermometry, reaction textures, and phase equilibria provide P-T limits for the peak conditions of biotite schist metamorphism. Sillimanite stability in meta-argillite horizons indicates peak conditions at least locally exceeding the minimum temperature of sillimanite stability at ~ 475 °C. The stability of peak assemblages (a) and (b) along with textural evidence for reaction (1) indicate peak metamorphic temperature between 600 and 650 ˚C, below the upper limit of muscovite stability defined by Evans and Guidotti (1966).

Garnet compositional profiles display a lack of zonation indicating porphyroblasts completely equilibrated at peak conditions and preserve no prograde growth history. Garnet-biotite temperatures record metamorphism between 420 and 620 °C. These

observations are consistent with peak P-T conditions in the middle amphibolite-facies, at 3 – 5 kbar, near 600 °C.

A critical question related to the limits of metamorphism regards the potential for biotite schist anatexis as a means to produce VGC melts. Anatexis is dependent on the presence of an aqueous fluid phase in a metamorphic system, which lowers the temperature required for the production of a partial melt. The activity of water in metamorphic systems is governed by dehydration reactions and the stability of mineralogic reservoirs. Along a prograde path, muscovite breakdown by reaction (2) at ~ 650 ˚C is generally the first major dehydration reaction which liberates sufficient water to induce anatexis. Because muscovite stability is widespread in the complex, textural evidence is lacking for reaction (2), and temperatures were likely below 650 ˚C, an aqueous fluid phase was likely absent and potential for anatexis extremely low.

The estimated peak conditions in the middle amphibolite-facies are achieved along a Barrovian-like medium P/T metamorphic trajectory (Figure 18). This medium P-T path likely corresponds to a geothermal gradient induced by burial. At 2.7 Ga, the P/T slope of this trajectory may actually be shallower, as the geotherm of the younger and hotter Archean crust was elevated. The nature of the Archean geotherm is debated (Rey and Houseman, 2006), thus the range of P-T trajectories related to Archean burial metamorphism remains enigmatic. Regardless of this uncertainty, other regimes of metamorphism are unlikely because these rocks lack critical assemblages. For example, the absence of high pressure phases such as glaucophane, omphacite, and abundant kyanite preclude metamorphism by subduction or collision. The stability of kyanite as reported by Tabor (1988) is possible over an interval along the trajectory plotted in Figure 18 as

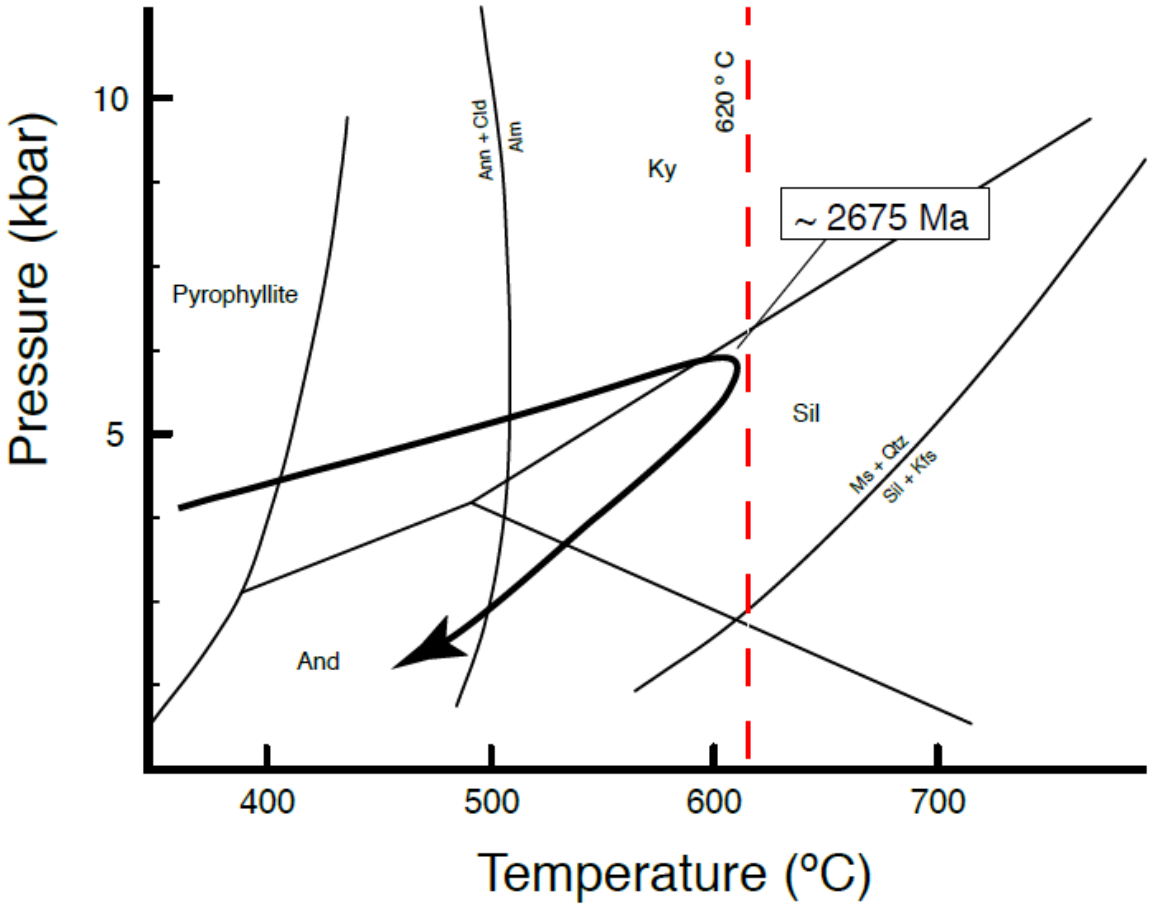

Figure 18. P-T-t path responsible for biotite schist metamorphism. The path follows a medium-P/T slope related to burial metamorphism. Equilibria after Spear and Cheney (1989). The red line shows the upper temperature limit of metamorphism obtained from garnet-biotite thermometry. Monazite mean age of ~ 2675 is inferred to record the time of peak metamorphism.

conditions likely were above the aluminosilicate triple point. Kyanite was likely replaced by sillimanite in most cases with advancing temperatures. Metamorphism along a low P/T trajectory is also unlikely as low pressure phases such as andalusite and high temperature phases such as cordierite are absent. The occurrence of sillimanite in the biotite schist as the peak Al_2SiO_5 phase is consistent with the paragenesis expected along a medium P-T Barrovian path.

The geographic distribution of sample locations in this study for which I determined the grade of metamorphism does not indicate the presence of a metamorphic field gradient, in contrast to the conclusions of Tabor (1988). Tabor (1988) mapped two metamorphic zones in the VCG. That work describes kyanite assemblages at localities in the Black Bay area and on the northern shores of the Kabetogama peninsula. Tabor (1988) mapped an isograd separating these sites from the sillimanite assemblages of the central and southern VGC rocks. I find sillimanite as the only Al_2SiO_5 phase in the VGC and document its occurrence as widespread throughout the complex. Furthermore, sillimanite occurs at a locality within the high pressure zone bounded by Tabor's (1988) kyanite isograd. Sample VGC-25-16 collected from the Black Bay Narrows contains fibrolite, M1b muscovite, and records a garnet-biotite temperature of ~ 475 ˚C. These temperature conditions constitute the lower limits of sillimanite stability.

As with the mineral assemblages, the geographic distribution of garnet-biotite temperatures does not indicate the presence of a metamorphic field gradient (Figure 19). Localized high temperatures in the biotite schist may have been induced around large granitic intrusions. Field observations show the lepidoblastic foliation of the biotite schist becomes increasingly well-defined near large bodies of LLCG, defining aureoles likely

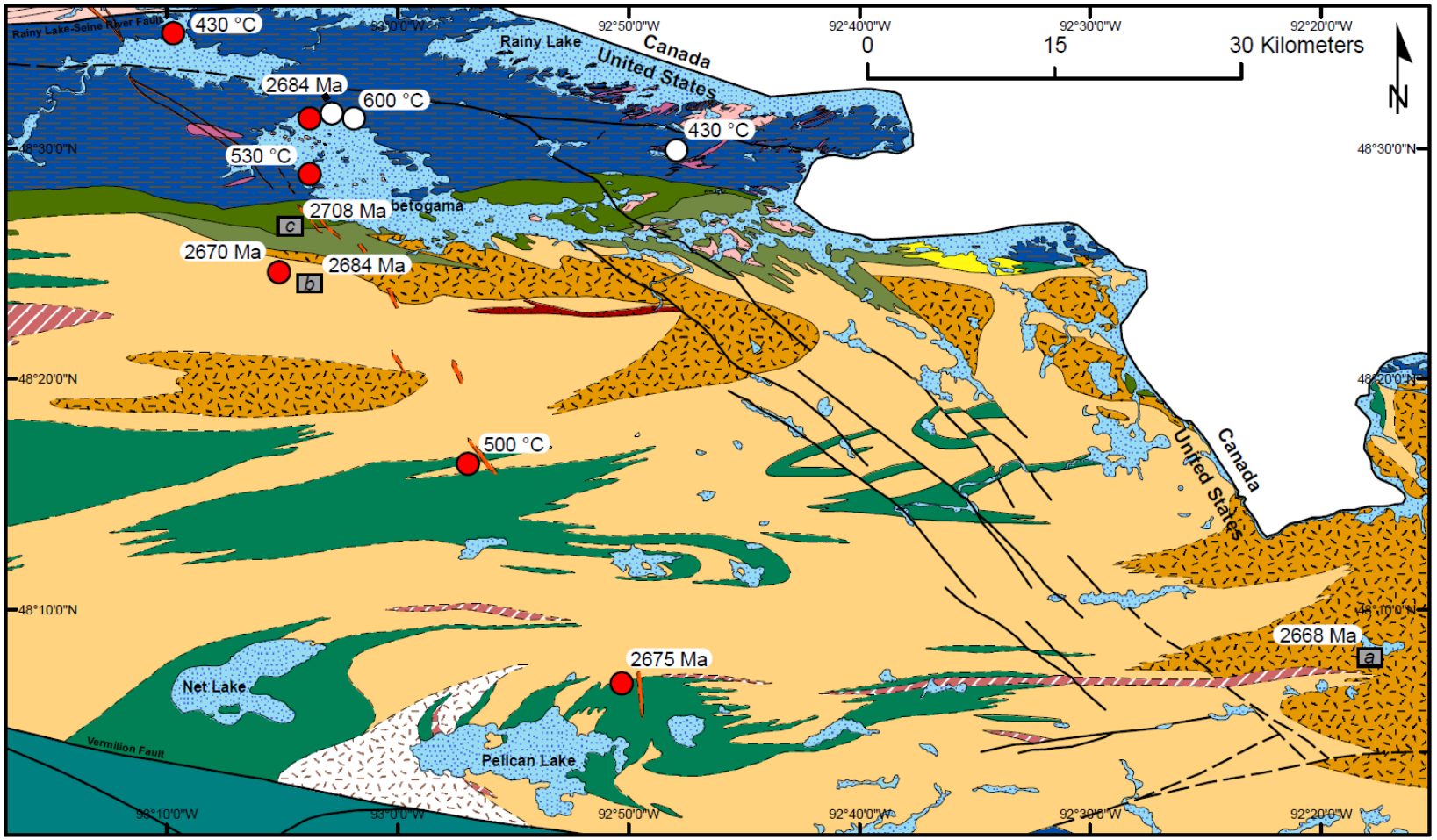

Figure 19. Map showing the locations of monazite ages in biotite schist, occurrence of sillimanite (indicated by red dots), and garnet-biotite temperatures of biotite schist metamorphism. Grey boxes indicate the locations of granitic rocks with zircon ages; *a* LLCG, *b* granodiorite, *c* leucogranite. Geologic units as in Figure 2. Note, temperatures are slightly elevated within proximity of the migmatized rocks and granitic bodie

induced locally by conductive heating by intrusions. No temperature data exist to further support this intrusion-country rock interaction. Broadly, metamorphism of the biotite schist to the amphibolite facies was likely accommodated along a Barrovian P-T trajectory. These conditions and style of metamorphism explain the P-T evolution of the VGC metasupracrustal rocks.

Peak metamorphic conditions and lepidoblastic fabric formation are temporally constrained by monazite U-Pb ages. The representative ages of the monazite-bearing samples are 2684 ± 14 Ma, 2670 ± 11 Ma, and 2676 ± 18 Ma. The two latter ages are the weighted-mean of several $^{207}Pb/^{206}Pb$ ages, whereas the age of 2784 ± 14 Ma is a concordia age calculated for a single analysis. Thus, peak metamorphism is confidently estimated at ~ 2675 Ma, from the two weighted-mean ages.

7.3 Origin of the leucogranite

Complex leucogranite zircon U-Pb age data can fit an upper intercept age of 2708 ± 94 Ma, regarded as the timing of leucogranite crystallization. Pervasive stromatic migmatite structures with leucogranite and peraluminous minimum melt-like leucosome provide evidence of a leucogranite source by partial melting of biotite schist. Day and Weiblen (1986) detailed the geochemical relationship between modeled compositions of biotite schist partial melts and leucogranite composition. They postulated the expected REE composition of a biotite schist partial melt at different degrees of melting. These models only reproduced REE compositions similar to actual leucogranite values at high degrees of partial melting and with a modification of the biotite schist bulk composition to include 5% modal hornblende. As found in this study, amphibole in the VGC biotite schist

is tschermakite and is not a major mineralogic constituent of the biotite schist, being localized to only metavolcanosedimentary horizons. Therefore, the geochemical models by Day and Weiblen (1986) may overestimate the modal proportion of available amphibole in schist to explain the relationship. Furthermore, the middle amphibolite-facies peak P-T indicated in this study is unlikely to induce partial melting to form leucogranite. It is more plausible that leucogranite was sourced from an external magmatic system, and intruded into biotite schist.

The geochemical similarities between the leucogranite and biotite schist may be explained to some degree by compositional mixing between injected leucogranite and the biotite schist. At outcrop, textural evidence for mixing is the dissociation of biotite schist melanosome into leucogranite leucosome. Sillimanite and monazite, common metamorphic minerals in the biotite schist, occur in leucogranitic rocks west of the VGC in the Quetico subprovince (Percival and Sullivan 1988). Leucogranite monazites dated by Percival and Sullivan (1988) yielded $^{207}Pb/^{206}Pb$ ages of 2665 ± 2 Ma, within error of schist monazites ages reported herein. Thus, leucogranite sillimanite, monazite, and garnet are likely xenocrystic from the biotite schist. Accessory mineral xenocrysts along with the geochemical similarities reported by Day and Weiblen (1986) are good evidence for some degree of mixing between the biotite schist and an injected leucogranite melt.

Although the available zircon age data for the timing of leucogranite crystallization are imprecise and within error of the metamorphic monazite ages, field observations indicate that metamorphism and injection were not synchronous. The lepidoblastic fabric of the biotite schist is cross-cut by leucogranite dikes (Figure 8), indicating that injections are post-metamorphic.

7.4 Origin of the Lac La Croix Granite

Dikes of LLGC in schist and rafted migmatite structures are intrusive features. The migmatitic interface between the biotite schist and LLCG is characterized by an increase in both dike volume and leucosome abundance approaching the granitic core of the complex. Contact metamorphic aureoles around large bodies of LLCG are defined by a localized increase in the degree of biotite schist foliation.

Low initial $^{87}Sr/^{86}Sr$ ratios of about 0.7004 reported by Peterman et al. (1972) and Jahn and Murthy (1975) for the LLCG suggest a short crustal residence time for the source of LLCG melt. An older melt source, with a more evolved Rb-Sr isotope system having been removed from the mantle earlier, would produce a melt with a higher initial $^{87}Sr/^{86}Sr$ ratio. Initial LLCG $^{87}Sr/^{86}Sr$ values are representative of a melt source with a crustal residence time of less than 50 Ma (Day and Weiblen 1986). Strontium values for the LLCG are inconsistent with biotite schist as the melt source material, as VGC metasupracrustals are composed of material derived from 2690-3250 Ma terrains. Further, the production of melt during metamorphism, let alone the production of the massive volume of LLCG in the complex is inconsistent with the peak P-T estimated here. The voluminous bodies of LLCG are rather likely sourced from outside of the complex and are not the melt products of the reworking of supercrustal rocks. Open system behavior characterizes the evolution of the VGC as the LLCG was likely source externally. The plutonic history of the complex is characterized by the intrusion of new felsic rock, distilled from recently extracted mantle material.

U-Pb analyses of complex multidomainal LLCG zircons contributes to the uncertainty regarding the timing of LLCG crystallization and emplacement. The multiple

oscillatory domains within LLCG zircons indicate polyphase crystallization in a dynamic magmatic system. Regression of U-Pb data along a Pb-loss trajectory yields an upper intercept age at 2722 ± 68 Ma. The $^{207}Pb/^{206}Pb$ age of the most concordant analysis is within error of the intercept age at 2668 ± 10 Ma. Contact aureoles and cross-cutting relationships indicate that the emplacement of the LLCG was post-metamorphic, and strontium isotope compositions indicate that melts were derived from a lower crustal or mantle source.

7.5 Origin of the granodiorite

The granodiorite is in contact with biotite schist as large voluminous dikes adjacent to bodies of LLCG. A higher modal plagioclase content distinguishes the granodiorite from the LLCG. The close proximity between these units and their mineralogic similarity indicates a possible genetic relationship between the LLCG and granodiorite. The granodiorite melt appears to be less-evolved, indicated by a higher plagioclase component. The intrusion of these less-evolved bodies predated the emplacement of later, more evolved LLCG melts. The mean granodiorite intercept age of 2684 ± 23 Ma predates the $^{207}Pb/^{206}Pb$ age of the most concordant LLCG zircon at 2668 ± 10 Ma, although they are within uncertainty of one another.

7.6 The style and tempo of crustal evolution in the Vermilion Granitic Complex

The Neoarchean is commonly regarded to be characterized by the most rapid rates of net crustal growth, more so than at any other point in geologic time. The short time interval for development of crust comprising the VGC is evidence of these rapid rates. Metamorphic constraints eliminate the potential for anatexis as the source of granitic rock

in the VGC. Any VGC petrogenetic interpretation must regard the complex as an open system in which granitic rocks were emplaced from external sources. The plutonic phases are new additions to the crust, being melt products from rock recently removed from the mantle rather than derivatives from existing metasupracrustals. Thus, plutonic rocks were juvenile to the crust and the plutonic evolution of the VGC can be viewed fundamentally as a crustal growth process.

The diverse distribution of detrital zircon ages indicates the growth of crust in the sediment source terrain may have operated much like the melt injection driven growth of the VGC. Major detrital age peaks may record five periods of emplacement of large juvenile felsic plutonic material within the sediment source region within ~ 150 Ma. The weathering of the plutonic bodies was likely soon after crystallization, as the youngest detrital ages are only ~ 15 Ma older than the age of biotite schist peak P-T at ~2675 Ma (Figure 20). Sedimentation seems to have been rapid, and quickly filled proximal basins, inducing metamorphic conditions at the base of the sedimentary pile to the middle amphibolite-facies. Emplacement of the earliest granitic intrusions postdated the development of the lepidoblastic biotite schist fabric, as indicated by cross-cutting relationships. The main intrusion of the LLCG was at about 2670 Ma, within ~ 5 Ma of peak metamorphism (Figure 20). The other varieties of granitic rock in the VGC are likely related to the LLCG magmatic system. Granitoids of more granodioritic composition may be earlier intrusions of a slightly less evolved melt from the LLCG system. Leucogranitic rocks are peraluminous, possibly a result of LLCG-biotite schist mixing or a further evolved product of the LLCG melt. Although constraints do not establish the magmatic

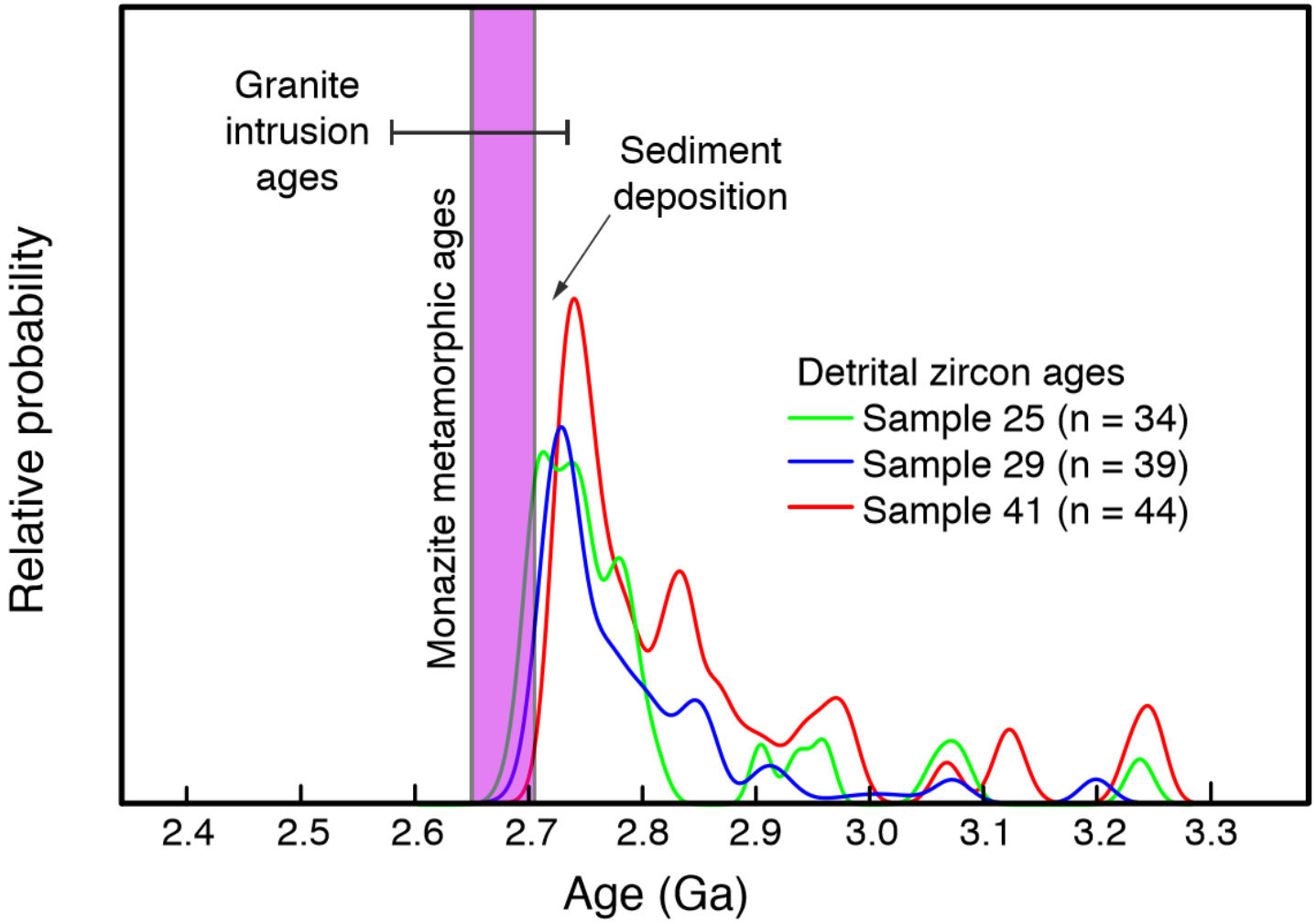

Figure 20. Comparison of detrital zircon $^{207}Pb/^{206}Pb$ ages from biotite schist with metamorphic monazite and igneous zircon U-Pb crystallization ages. The inferred interval of deposition is noted, bracketed by the youngest detrital zircon $^{207}Pb/^{206}Pb$ age and monazite crystallization. Detrital data plotted includes $^{207}Pb/^{206}Pb$ ages of all reliable biotite schist zircon analyses.

processes responsible for the variety of VGC granitic rocks, field observations and geochronology indicate that granitoids may be genetically related and sourced from the same intrusive magmatic system.

The minimum interval for the total sedimentary-metamorphic-plutonic history of the VGC is accommodated in ~ 30 Ma (Figure 20). In relation to rates and styles of Neoarchean crustal growth, I find during the ~ 30 Ma evolution of the ~ 6,500 km^2 VGC that ~ 70% of the crustal material exposed in the complex was newly sourced melt from the mantle. Broadly, the ~ 30 Ma evolution of the VGC may be one component of a larger rapidly growing system. Detrital age pulses at ~ 2700, ~ 2710, ~ 2715, ~ 2750, and ~ 2850 Ma are likely a record of the crystallization of other major juvenile Neoarchean plutonic bodies in the region, also possible significant events of crustal growth. Rapid crustal evolution is not limited to the VGC, but seems to characterize the growth of the greater Quetico belt. Existing detrital and plutonic age constraints for eastern Quetico rocks are consistent with ages in the VGC (Percival and Sullivan, 1988; Davis et al., 1990). Thus, the style of VGC formation evidenced by these data may provide insight into the formation of the greater Quetico belt.

8 Conclusions

The rocks of the Vermilion Granitic Complex in the western Quetico belt record the deposition of a greywacke protolith until ~ 2690 Ma. Subsequently, burial induced Barrovian-style metamorphism to amphibolite facies, with peak conditions at ~ 2675 Ma. Granitic melts distilled from recently removed mantle material intruded during and after metamorphism. The total sedimentary-metamorphic-plutonic evolution of the complex may have been completely accommodated in a brief ~ 30 Ma interval.

Crustal growth rates during the Neoarchean transition are argued to have been the most rapid in geologic time. My findings illustrate 1) the plutonic evolution of the complex to be driven by new crustal growth and 2) the rate of deposition-metamorphism-plutonism to be of short duration. Therefore, the tempo of these processes in the VGC may be a general analogue for crustal growth rates and processes operating during the Neoarchean transition.

References cited

Anderson, D. L., 1987, Thermally induced phase changes, lateral heterogeneity of mantle, continental roots, and deep slab anomalies, Journal of Geophysical Research, v. 90, p. 13965-13980.

Card, K. C., and Ciesielski, A., 1986, Subdivisions of the Superior province of the Canadian Shield, Geoscience Canada, v. 13, p. 5-13.

Condie, K. C., 1981, Archean Greenstone Belts: Amsterdam, Elsevier Scientific Publishing Company, 434 pg.

Condie, K. C., 1998, Episodic continental growth and supercontinents: a mantle avalanche connection?, Earth and Planetary Science Letters, v. 193, p. 97-108.

Condie, K. C., 1994, Greenstones through time, *in* Archean Crustal Evolution, *ed* Condie, K. C., Elsevier, Amsterdam, p. 85-120.

Condie, K. C., 2007, Accretionary origins in space and time, *in* 4-D Framework of Continental Crust, *ed* Hatcher, R. D., Carlson M. P., McBride, J. H., Geological Society of America Memoir, v. 200, p. 145-158.

Condie, K. C., and Kröner, A., 2013, The building blocks of continental crust: Evidence for a major change in the tectonic setting of continental growth at the end of the Archean, Gondwana Research, v. 23, p. 394–402.

Corfu, F., Hanchar, J., Hoskin, P., Kinny, P., 2003, Atlas of zircon textures, *in* Zircon, *ed* Hanchar, J., Hoskin, P., Reviews in mineralogy and geochemistry, v. 53, p. 469-495.

Davis, D. W., Pezzutto, F., Ojakangas, R. W., 1990, The age and provenance of metasedimentary rocks in the Quetico subprovince, Ontario, from single zircon analyses: implications for Archean sedimentation and tectonics in the Superior province, Earth and Planetary Science Letters, v. 99, p. 195-205.

Day, W. C., 1983, Petrology and geochemistry of the Vermilion Granitic Complex, northern Minnesota [Ph.D. dissertation], University of Minnesota, 192 pg.

Day, W. C., Weiblen, P., 1986, Origin of Late Archean Granite: Geochemical evidence from the Vermilion Granitic Complex of northern Minnesota, Contributions to Mineralogy and Petrology, v. 93, p. 283-296.

Easton, M. R., 2000, Metamorphism of the Canadian Shield, Ontario Canada, 1 the Superior Province, The Canadian Mineralogist, v. 38, p. 287-317.

Ernst, W. G., Sleep, N. S., Tsujimori, T., 2016, Plate-tectonic evolution of the Earth: bottom-up and top-down mantle circulation, Canadian Journal of Earth Sciences, v. 53, p. 1103-1120.

Evans, B. W. and Guidotti, C. V., 1966, The sillimanite-potash feldspar isograd in western Maine, U.S.A, Contributions to Mineralogy and Petrology, v. 12, p. 25-62.

Ferry, J.M. and Spear, F.S., 1978, Experimental calibration of the partitioning of Fe and Mg between biotite and garnet, Contributions to Mineralogy and Petrology, v. 66, p. 113–117.

Hawkesworth, C., Kemp, A., 2006, Evolution of the continental crust, Nature, v. 443, p. 811-817.

Hemstad, C. B., Southwick, D. L., Ojakangas, R. W., compilers, 2002, Bedrock geological map of Voyagers National Park and vicinity, Minnesota, Minnesota Geological Survey, scale 1:50,000, 1 sheet.

Hoskin, P. and Schaltegger, U., 2003, The composition of zircon and igneous and metamorphic petrogenesis, *in* Zircon, *ed* Hanchar, J., Hoskin, P., Reviews in mineralogy and geochemistry, v. 53, p. 27-55.

Jahn, B., Murthey, V. R., 1975, Rb-Sr ages of Archean rocks from the Vermilion district, northeastern Minnesota, Geochemica et Cosmochimica Acta, v. 39, p. 1679-1689.

Ludwig, K.R., 1999. Using Isoplot/Ex, Version 2.01: a geochronological toolkit for Microsoft Excel, Berkeley Geochronology Center Special Publication, n. 1a: 47.

Martin H., 1994, Archean Grey Gneisses and the Genesis of Continental Crust, in, Condie K. C., Archean Crustal Evolution, p. 205-247.

Menhert, K. R., 1968, Migmatites and the origin of granitic rocks, Elsevier, Amsterdam.

Ojakangas, R. W., 1985, Review of Archean clastic sedimentation, Canadian Shield: Major felsic volcanic contributions to turbidite and alluvial fan-fluvial facies associations, *in* Evolution of Archean supercrustal sequences, *ed* Ayers, L. D., Thurston, P. C., Card, K. D., Weber W., p. 23.

Pan, Y., Fleet, M., 1999, Kyanite in the western Superior Province of Ontario: implications for Archean accretionary tectonics, The Canadian Mineralogist, v. 37, p. 359-373.

Percival, J. A., 1988, A regional perspective of the Quetico metasedimentary belt, Superior Province, Canada. Canadian Journal of Earth Sciences. v. 26, no. 4, p. 677-693.

Percival, J. A., and Sullivan, R. W., 1988, Age constrains on the evolution of the Quetico belt, Superior province, Ontario, in Radiogenic and isotopic studies: report 2, Geologic Survey of Canada, paper 88-2, p. 97-107.

Peterman Z. E., Goldich S. S., Hedge C. E., Yardley D. H., 1972, Geochronology of the Rainy Lake Region, Minnesota Ontario, Geological Society of America Memoir, no. 135, p. 193-216.

Poulsen, H. K., Borradalie, G. J., Khellenback, M., 1980, Inverted Archean succession at Rainy Lake, Ontario. Canadian Journal of Earth Sciences, v. 17, p. 1358-1369.

Rye, D., Roy, R., 1978, The distribution of thorium, uranium and potassium in Archean granites from northeastern Minnesota, American Journal of Science, v. 278, p. 354-378.

Rey, P., Houseman, G., 2006, Lithospheric scale gravitational flow: the impact of body forces on orogenic processes from Archean to Phanerozoic, *in* Analogue and Numerical Modeling of Crustal-Scale Processes, *ed* Buiter, H., Schreurs, G., v. 253, p. 153-167.

Southwick, D. L., 1972, Vermilion granite-migmatite massif, *in* Geology of Minnesota: a centennial volume, *ed* Sims, P. K., and Morey G. B., Minnesota Geological Survey, St. Paul, p. 108-119.

Southwick, D. L., Ojakangas, R. W., compilers, 1979, Geologic map of Minnesota International Falls sheet, Minnesota Geological Survey, scale 1: 250,000, 1 sheet.

Southwick D. L., Sims, P. K., 1980, The Vermilion Granitic Complex – a new name for old rocks in northern Minnesota, USGS professional paper 1124-A, A1-A11.

Spear, F.S., and Cheney, J.T., 1989, A petrogenetic grid for pelitic schists in the system SiOr-AlrO3-FeO-MgO-KrO-HrO, Contributions to Mineralogy and Petrology, v. 101, p. 149-164.

Sawyer, E. W., 2008, Atlas of Migmatites, NRC Research Press, Ottawa.

Tabor, J. R., Hudleston, P. J., 1991, Deformation at an Archean subprovince boundary, northern Minnesota, Canadian Journal of Earth Sciences, v. 28, no. 2, p. 292-307.

Thurston, P. C., 1991, Archean geology of Ontario, *in* Geology of Ontario, *ed* Thurston, P. C., Williams, H. R., Sutcluffe, R. H., Stout, G. M., p. 73.

Williams H. R., 1991, The Quetico Subprovince, *in* Geology of Ontario, *ed* Thurston, P. C., Williams, H. R., Sutcluffe, R. H., Stout, G. M, p. 383.

Appendices

Appendix A. Sample locations and field descriptions

Sample Number	Latitude	Longitude	Lithologic description
VGC-01-16	48.135067	-92.51901	Migmatite with large bodies of granitic neosome material in Bt-schist, ptygmatic folds of neosome within schist foliation
VGC-02-16	48.132337	-92.296985	LLCG
VGC-03-16	48.261513	-92.570712	Migmatite with large bodies of granitic neosome material in Bt-schist, ptygmatic folds of neosome within schist foliation
VGC-04-16	48.331766	-92.576851	LLCG
VGC-05-16	48.337325	-92.576851	Bt-schist granite migmatite (poor exposure)
VGC-06-16	48.480755	-93.061207	Bt-schist migmatite with pegmatitic neosome, 30% neosome
VGC-07-16	48.595318	-93.155696	Bt-schist
VGC-08-16	48.44116	-93.07671	Bt-schist blocks rafted in leucogranite neosome
VGC-09-16	48.40898	-93.08528	Amphibolite migmatite 20% pink granitic neosome
VGC-10-16 (ABC)	48.4106	-93.086	Bt-schist leucograntie and LLCG migmatite, 60% neosome, (A) leucogranite (B) LLCG (C) Hbl-Bt schist
VGC-11-16	48.37737	-92.820352	Bt-schist grantie migmatite, 15% stromatic neosome with foliation
VGC-12-16	48.389677	-92.806096	Quartz diorite
VGC-13-16	48.403492	-92.811212	Granite
VGC-14-16	48.406225	-92.80657	Bt-schist granite migmatite with 15% ptygmatic neosome with foliation
VGC-15-16	48.393399	-92.869915	Bt-schist granite migmatite, 20% neosome
VGC-16-16	48.484226	-93.057478	Bt-schist granite migmatite, 5% neosome
VGC-17-16	48.41061	-93.08601	Stromatic Bt-schist migmatite, 90% neosome

Sample Number	Latitude	Longitude	Lithologic description
VGC-18-16	48.33705	-92.96283	Diorite
VGC-19-16	48.41061	-93.08601	Bt-schist granite migmatite with large intrusions of granite
VGC-20-16	48.212492	-92.904837	Bt-schist granite stromatic migmatite, 50% neosome
VGC-21-16	48.05895	-92.83073	Bt-schist granite migmatite, 30% neosome
VGC-22-16	48.07399	-92.978218	Quartz diorite
VGC-23-16	48.44115	-93.07676	Bt-schist blocks rafted in leucogranite neosome
VGC-24-16	48.39976	-92.836817	Bt-schist granite stromatic migmatite, 30% neosome
VGC-25-16 (AB)	48.58285	-93.16047	Bt-schist, (A) micaceous horizon (B) quartzofeldspathic horizon
VGC-26-16 (AB)	48.421659	-92.846114	Bt-schist granite migmatite, 20% neosome (A) bt-schist (B) granite
VGC-27-16	48.434798	-92.849871	Bt-schist granite migmatite, 20% neosome
VGC-28-16	48.46575	-92.84084	Bt-schist granite migmatite, 10% neosome
VGC-29-16	48.4651	-92.83961	Bt-schist granite migmatite with large intrusions of granite
VGC-30-16	48.5196	-92.77195	Bt-schist with intrusive pegmatitic dikes
VGC-31-16	48.49826	-92.7957	Bt-schist with intrusive pegmatitic dikes
VGC-32-16	48.37691	-92.82062	Bt-schist granite migmatite, 15% neosome with foliation
VGC-33-16	48.52355	-93.04147	Bt-schist with intrusive pegmatitic dikes
VGC-34-16 (AB)	48.52477	-93.0468	Bt-schist with intrusive pegmatitic dikes, (A) leucogranite (B) Bt-Schist
VGC-36-16 (AB)	48.52681	-93.05562	Bt-schist with intrusive pegmatitic dikes, (A) leucogranite (B) Bt-Schist

Sample Number	Latitude	Longitude	Lithologic description
VGC-37-16 (AB)	48.52171	-93.03145	Bt-schist with intrusive pegmatitic dikes, (A) leucogranite (B) Bt-Schist
VGC-38-16	48.525703	-93.027874	Bt-schist
VGC-39-16	48.48304	-93.06354	Bt-schist
VGC-40-16 (AB)	48.27186	-92.94857	Bt-schist granite migmatite with large intrusions of granite, (A) granite (B) Bt-Schist
VGC-41-16 (AB)	48.21256	-92.90492	Bt-schist granite migmatite, 10% neosome, (A) granite (B) Bt-schist
VGC-42-16	48.11207	-92.84004	Bt-schist with intrusive pegmatitic dikes
VGC-43-16 (AB)	48.2615	-92.57079	Migmatite with large bodies of granitic neosome intruding bt-schist, ptygmatic folds of neosome within schist foliation, (A) granite (B) bt-schist
VGC-44-16	48.13239	-92.29695	LLCG
VGC-45-16	48.07453	-92.66982	Bt-schist granite migmatite, 20% neosome
VGC-46-16 (AB)	48.00178	-92.83034	Bt-schist granite migmatite, 30% neosome, (A) granite (B) Bt-schist
VGC-48-16	48.408965	-93.084188	Granodiorite cross-cutting stromatic migmatite

Appendix B. WDS standards

Phase	Standard	For element
Anorthite	NMNH 137041	Ca
Chromite	NMNH 117075	Cr
Hornblende	NMNH 143965 (Kakanui)	Si
Ilmenite	NMNH 96189	Ti, Fe
Tugtupite	CIT-8080, GRR153	Cl
Pyrope	Frank Smith	Al, Mg
Spessartine	Verma	Mn
Orthoclase	Taylor	K
Albite	Taylor	Na

Appendix C. Geochronology standards

Phase	*Standard*	*Frequency*
Zircon	Plešovice	6 for every 10 unkowns
Zircon	FC-1	2 for every 10 unkowns
Zircon	95100	1 for every 10 unkowns
Monazite	Trebilcock	3 every 2 unkowns

Appendix D. Detrital zircon isotope data

Analysis	Th/U	Radiogenic ratios						Ages (Ma)						% Discordant
		$^{207}Pb/^{235}U$	±	$^{206}Pb/^{238}U$	±	$^{207}Pb/^{206}Pb$	±	$^{207}Pb/^{235}U$	±	$^{206}Pb/^{238}U$	±	$^{207}Pb/^{206}Pb$	±	
SAMPLE VGC-25-16														
25-1C	0.29	10.2797	0.2785	0.3969	0.0100	0.1878	0.0018	2460	25	2155	46	2723	16	21
25-1R	0.13	12.5011	0.2902	0.4625	0.0099	0.1960	0.0016	2643	22	2451	43	2793	14	12
25-2C	0.28	9.7509	0.2462	0.3652	0.0087	0.1936	0.0014	2412	23	2007	41	2773	12	28
25-2R	0.30	6.7010	0.1742	0.2404	0.0056	0.2021	0.0023	2073	23	1389	29	2844	19	51
25-3C	0.34	15.1412	0.3648	0.5847	0.0129	0.1878	0.0017	2824	23	2968	52	2723	15	-9
25-3R	0.48	7.9924	0.1996	0.2981	0.0069	0.1944	0.0018	2230	22	1682	34	2780	15	40
25-4C *	0.33	13.1877	0.3253	0.5102	0.0114	0.1874	0.0019	2693	23	2657	49	2720	16	2
25-4R	0.80	6.7259	0.1790	0.2441	0.0060	0.1998	0.0019	2076	23	1408	31	2825	15	50
25-5C	0.48	13.6489	0.3370	0.5362	0.0121	0.1846	0.0018	2726	23	2767	51	2694	16	-3
25-5R	0.37	13.6737	0.3175	0.5339	0.0115	0.1857	0.0015	2727	22	2758	48	2705	13	-2
25-6C	0.38	5.2911	0.1375	0.1987	0.0048	0.1934	0.0017	1867	22	1169	26	2772	14	58
25-6R	0.36	10.0382	0.2168	0.3877	0.0076	0.1881	0.0016	2438	20	2112	35	2726	14	23
25-7C	0.14	2.1663	0.0568	0.0673	0.0016	0.2339	0.0024	1170	18	420	10	3079	16	86
25-7R	0.22	22.2286	0.4661	0.6187	0.0118	0.2610	0.0021	3194	20	3105	47	3253	13	5
25-8C	0.60	13.4863	0.2614	0.5051	0.0089	0.1940	0.0014	2714	18	2636	38	2776	12	5
25-8R	0.35	10.9186	0.2517	0.4180	0.0084	0.1898	0.0021	2516	21	2251	38	2740	18	18
25-9C	0.55	20.0746	0.4392	0.6272	0.0124	0.2326	0.0020	3095	21	3139	49	3070	14	-2
25-9R	0.45	19.9650	0.4201	0.6158	0.0117	0.2356	0.0019	3090	20	3093	47	3090	13	0
25-10C	0.15	13.3155	0.2620	0.5185	0.0092	0.1866	0.0014	2702	18	2693	39	2712	13	1
25-10R	0.28	10.8057	0.2181	0.4115	0.0075	0.1908	0.0014	2507	19	2222	34	2749	12	19
25-11C	0.88	18.1358	0.3081	0.6070	0.0094	0.2182	0.0013	2997	16	3058	38	2967	10	-3
25-11R	1.06	6.1159	0.1269	0.1809	0.0033	0.2469	0.0023	1993	18	1072	18	3165	14	66

Analysis	Th/U	Radiogenic ratios						Ages (Ma)						% Discordant
		$^{207}Pb/^{235}U$	±	$^{206}Pb/^{238}U$	±	$^{207}Pb/^{206}Pb$	±	$^{207}Pb/^{235}U$	±	$^{206}Pb/^{238}U$	±	$^{207}Pb/^{206}Pb$	±	
25-12C	0.19	9.9427	0.2140	0.3822	0.0071	0.1900	0.0021	2429	20	2087	33	2742	18	24
25-12R	0.18	4.3382	0.0851	0.1628	0.0030	0.1946	0.0012	1701	16	972	17	2781	10	65
25-13C	0.24	7.8128	0.1584	0.2998	0.0054	0.1903	0.0018	2210	18	1690	27	2745	15	38
25-13R	0.09	10.4928	0.1961	0.4071	0.0069	0.1882	0.0014	2479	17	2202	31	2727	12	19
25-14C	0.36	13.3731	0.2243	0.5120	0.0078	0.1908	0.0011	2706	16	2665	33	2749	10	3
25-14R	0.29	6.6391	0.1327	0.2480	0.0044	0.1955	0.0017	2065	17	1428	23	2789	14	49
25-15C	0.43	17.0257	0.2880	0.5905	0.0092	0.2106	0.0012	2936	16	2991	37	2910	10	-3
25-15R	0.22	9.4141	0.2125	0.3197	0.0068	0.2150	0.0015	2379	21	1788	33	2944	11	39
25-16C	0.25	7.7998	0.2193	0.3038	0.0075	0.1874	0.0025	2208	25	1710	37	2720	22	37
25-16R	0.25	2.7771	0.0684	0.1044	0.0023	0.1942	0.0021	1349	18	640	13	2778	18	77
25-17C	0.27	13.8553	0.2620	0.5441	0.0094	0.1859	0.0013	2740	18	2800	39	2706	11	-3
25-17R	0.28	12.0809	0.2284	0.4737	0.0082	0.1861	0.0012	2611	18	2500	36	2708	11	8
25-18C	0.32	11.8808	0.2679	0.4539	0.0093	0.1911	0.0017	2595	21	2413	41	2751	15	12
25-18R	0.19	5.4957	0.1461	0.2121	0.0053	0.1892	0.0017	1900	23	1240	28	2735	15	55
25-19C	0.55	14.1392	0.2751	0.5389	0.0094	0.1915	0.0015	2759	18	2779	39	2755	13	-1
25-19R	0.60	10.8480	0.2122	0.4064	0.0074	0.1948	0.0013	2510	18	2199	34	2783	11	21
25-20C	0.31	4.6656	0.1263	0.1704	0.0043	0.1999	0.0020	1761	22	1014	23	2825	16	64
25-20R	0.26	4.1916	0.1185	0.1562	0.0043	0.1959	0.0013	1672	23	936	24	2792	11	66
25-21C	0.35	7.9964	0.1741	0.3021	0.0056	0.1925	0.0022	2231	19	1702	28	2764	18	38
25-21R	0.45	9.0940	0.1395	0.3497	0.0047	0.1892	0.0012	2348	14	1933	23	2735	10	29
25-22C	0.16	1.5041	0.0478	0.0413	0.0013	0.2651	0.0019	932	19	261	8	3277	11	92
25-22R	0.30	12.9909	0.2206	0.4378	0.0066	0.2158	0.0015	2679	16	2341	30	2950	12	21
25-24C	0.21	2.6527	0.0798	0.0926	0.0027	0.2084	0.0014	1315	22	571	16	2893	11	80
25-24R *	0.20	3.2217	0.0495	0.0924	0.0012	0.2537	0.0017	1462	12	570	7	3208	11	82
25-25C	0.26	1.9307	0.0548	0.0662	0.0018	0.2122	0.0014	1092	19	413	11	2923	10	86

Analysis	Th/U	Radiogenic ratios						Ages (Ma)						% Discordant
		$^{207}Pb/^{235}U$	±	$^{206}Pb/^{238}U$	±	$^{207}Pb/^{206}Pb$	±	$^{207}Pb/^{235}U$	±	$^{206}Pb/^{238}U$	±	$^{207}Pb/^{206}Pb$	±	
25-25R	0.61	12.8514	0.2198	0.4577	0.0071	0.2042	0.0013	2669	16	2429	31	2860	10	15
25-26C	0.80	9.4128	0.1609	0.3411	0.0052	0.2007	0.0014	2379	16	1892	25	2832	11	33
25-26R	0.39	6.6858	0.1306	0.2456	0.0045	0.1980	0.0012	2071	17	1416	23	2810	10	50
25-26R	0.16	6.6858	0.1306	0.2456	0.0045	0.1980	0.0012	2071	17	1416	23	2810	10	50
25-27C *	1.55	4.4248	0.1264	0.1532	0.0042	0.2103	0.0017	1717	23	919	23	2938	17	69
25-27R	1.70	5.2153	0.1231	0.1888	0.0042	0.2011	0.0017	1855	20	1115	22	2812	13	60
25-28C *	0.61	36.4777	1.1399	0.9382	0.0269	0.2832	0.0037	3679	30	4266	89	3370	21	-27
25-28R	0.53	13.6383	0.3010	0.5314	0.0109	0.1869	0.0014	2725	21	2747	46	2701	15	-2
25-29C	0.43	10.0083	0.2591	0.3882	0.0096	0.1877	0.0014	2436	24	2115	44	2730	14	23
25-29R	0.30	9.0813	0.2305	0.3460	0.0084	0.1912	0.0014	2346	23	1915	40	2737	23	30
SAMPLE VGC-29-16														
29-1C	0.11	6.4145	0.1435	0.2320	0.0048	0.2003	0.0018	2034	19	1345	25	2890	13	53
29-1R	0.24	11.7306	0.1991	0.4492	0.0070	0.1892	0.0012	2583	16	2392	31	2736	13	13
29-2C	0.47	11.3271	0.1971	0.4343	0.0069	0.1889	0.0013	2550	16	2325	31	2769	15	16
29-2R	0.50	13.9480	0.2528	0.5385	0.0091	0.1877	0.0012	2746	17	2777	38	2710	14	-2
29-3C	0.25	10.4955	0.2294	0.4009	0.0079	0.1897	0.0018	2480	20	2173	36	2725	14	20
29-3R	0.29	12.0770	0.2148	0.4662	0.0077	0.1877	0.0012	2610	17	2467	34	2721	13	9
29-5aC	0.25	6.8731	0.1395	0.2557	0.0047	0.1947	0.0017	2095	18	1468	24	2773	15	47
29-5aR *	0.21	7.4951	0.1365	0.2717	0.0046	0.1999	0.0014	2172	16	1549	23	2809	14	45
29-5bC	0.31	14.7926	0.2166	0.5628	0.0073	0.1901	0.0012	2802	14	2878	30	2742	14	-5
29-5bR	0.19	14.8528	0.2227	0.5617	0.0075	0.1913	0.0012	2806	14	2874	31	2736	13	-5
29-6aC *	0.50	38.2100	0.9354	1.0423	0.0248	0.2652	0.0015	3725	24	4603	78	3267	12	-41
29-6aR	0.17	9.4853	0.1619	0.3090	0.0047	0.2221	0.0017	2386	16	1736	23	2996	12	42
29-6bC	0.26	10.1705	0.1957	0.3669	0.0067	0.2005	0.0013	2450	18	2015	31	2819	13	29
29-6bR	0.15	6.8888	0.1472	0.2318	0.0045	0.2150	0.0020	2097	19	1344	24	3003	36	55
29-7C	0.13	13.6696	0.2563	0.5342	0.0087	0.1851	0.0018	2727	18	2759	36	2552	15	-8

Analysis	Th/U	Radiogenic ratios						Ages (Ma)						% Discordant
		$^{207}Pb/^{235}U$	±	$^{206}Pb/^{238}U$	±	$^{207}Pb/^{206}Pb$	±	$^{207}Pb/^{235}U$	±	$^{206}Pb/^{238}U$	±	$^{207}Pb/^{206}Pb$	±	
29-7R *	0.23	6.9788	0.1593	0.2567	0.0055	0.1967	0.0016	2109	20	1473	28	2788	15	47
29-8C	0.38	13.8620	0.2069	0.5433	0.0073	0.1846	0.0011	2740	14	2797	30	2685	13	-4
29-8R	0.35	11.2359	0.1838	0.4322	0.0065	0.1881	0.0011	2543	15	2315	29	2714	13	15
29-9aC	0.15	6.7840	0.2633	0.2605	0.0099	0.1884	0.0018	2084	34	1492	50	2763	15	46
29-9aR *	0.13	8.7440	0.3373	0.3253	0.0122	0.1944	0.0021	2312	35	1816	59	2865	15	37
29-9bC	0.39	12.9184	0.4679	0.5045	0.0180	0.1852	0.0014	2674	34	2633	77	2710	14	3
29-10C	0.32	10.4832	0.3891	0.3957	0.0145	0.1917	0.0014	2478	34	2149	67	2746	14	22
29-10C	0.32	11.1099	0.1880	0.3977	0.0060	0.1998	0.0015	2428	16	2105	26	2806	15	25
29-10R	0.32	12.4291	0.5344	0.4809	0.0195	0.1870	0.0029	2637	40	2531	84	2915	17	13
29-11C	0.38	12.9496	0.5003	0.5032	0.0191	0.1862	0.0016	2676	36	2627	81	2693	17	2
29-11R	0.44	13.4193	0.4964	0.4491	0.0161	0.2162	0.0022	2710	34	2391	71	3081	17	22
29-12C	0.18	11.8093	0.4468	0.4634	0.0172	0.1844	0.0015	2589	35	2454	75	2694	16	9
29-12R	0.03	3.4289	0.1236	0.0898	0.0032	0.2762	0.0021	1511	28	554	19	3334	18	83
29-13C	0.38	13.3329	0.6984	0.5175	0.0265	0.1866	0.0024	2704	48	2689	112	2728	23	1
29-13R	0.17	8.7933	0.4191	0.3325	0.0154	0.1916	0.0023	2317	43	1850	74	2751	22	33
29-14aC	0.14	3.0428	0.1626	0.1088	0.0057	0.2025	0.0020	1418	40	666	33	2762	14	76
29-14aR	0.17	9.6497	0.4472	0.3715	0.0171	0.1881	0.0014	2402	42	2037	80	2837	15	28
29-14bC	0.20	9.8953	0.4613	0.3652	0.0167	0.1962	0.0021	2425	42	2007	78	2839	18	29
29-14bR	0.03	3.7141	0.1668	0.1157	0.0052	0.2325	0.0015	1574	35	706	30	3065	13	77
29-15C	0.37	13.7950	0.6486	0.5367	0.0248	0.1862	0.0018	2736	44	2769	103	2732	17	-1
29-15R	0.35	10.8054	0.4955	0.4071	0.0185	0.1923	0.0015	2507	42	2201	84	2814	16	22
29-16C	0.40	12.1731	0.5622	0.4505	0.0207	0.1957	0.0013	2618	42	2398	91	2780	13	14
29-16R	0.22	7.3805	0.3805	0.2687	0.0137	0.1990	0.0020	2159	45	1534	69	2777	14	45
29-17C	0.28	13.0119	0.5525	0.5102	0.0213	0.1857	0.0015	2681	39	2657	90	2701	16	2
29-17R	0.24	12.0977	0.5071	0.4551	0.0188	0.1935	0.0015	2612	39	2418	83	2848	16	15
29-18C	0.33	11.9844	0.5498	0.4686	0.0209	0.1862	0.0020	2603	42	2477	91	2709	20	9

Analysis	Th/U	Radiogenic ratios						Ages (Ma)						% Discordant
		$^{207}Pb/^{235}U$	±	$^{206}Pb/^{238}U$	±	$^{207}Pb/^{206}Pb$	±	$^{207}Pb/^{235}U$	±	$^{206}Pb/^{238}U$	±	$^{207}Pb/^{206}Pb$	±	
29-18R	0.21	8.8235	0.4003	0.3375	0.0150	0.1903	0.0017	2320	41	1875	72	2745	18	32
29-19aC	0.43	12.5081	0.5209	0.4788	0.0196	0.1902	0.0015	2643	38	2522	85	2727	16	8
29-19aR	0.43	12.9266	0.5355	0.5048	0.0206	0.1864	0.0014	2674	38	2635	88	2703	15	3
29-19bC	0.45	13.5615	0.5523	0.5241	0.0211	0.1884	0.0012	2720	38	2716	88	2715	13	0
29-19bR	0.32	13.7494	0.6008	0.5451	0.0230	0.1836	0.0021	2733	41	2805	95	2615	14	-7
29-20C	0.36	11.6268	0.5654	0.4522	0.0213	0.1872	0.0024	2575	44	2405	94	2709	22	11
29-20R *	0.35	13.3122	0.6433	0.5217	0.0242	0.1858	0.0026	2702	45	2706	102	2753	27	2
29-21aC *	0.15	4.9336	0.1467	0.1555	0.0044	0.2318	0.0018	1808	25	932	25	3070	13	70
29-21aR	0.22	11.2942	0.3280	0.4352	0.0122	0.1897	0.0013	2548	27	2329	55	2730	13	15
29-21bC	0.44	12.6774	0.3711	0.5073	0.0143	0.1827	0.0013	2656	27	2645	61	2678	13	1
29-21bR	0.26	7.2439	0.2165	0.2695	0.0078	0.1965	0.0012	2142	26	1538	40	2803	17	45
29-22aC	0.63	13.2352	0.3797	0.4972	0.0138	0.1946	0.0012	2697	27	2602	59	0	0	0
29-22aR	0.08	6.9474	0.2082	0.2401	0.0069	0.2115	0.0017	2105	26	1387	36	2914	15	52
29-22bC	0.37	12.3467	0.3703	0.4844	0.0140	0.1863	0.0013	2631	28	2546	61	2702	14	6
29-22bR	0.26	6.5798	0.2506	0.2473	0.0089	0.1945	0.0023	2057	33	1424	46	2740	16	48
29-24C	0.23	11.5429	0.3357	0.4498	0.0126	0.1876	0.0013	2568	27	2394	56	2726	14	12
29-24R	0.10	7.5266	0.2485	0.2695	0.0086	0.2041	0.0015	2176	29	1538	44	2980	22	48
29-25C	0.33	13.1351	0.3306	0.5116	0.0123	0.1868	0.0013	2689	23	2664	52	2730	14	2
29-25R	0.27	8.4816	0.2221	0.3202	0.0080	0.1927	0.0015	2284	24	1791	39	2844	15	37
29-26C	0.33	13.8719	0.3495	0.5146	0.0125	0.1961	0.0012	2741	24	2676	53	2787	13	4
29-27C	0.40	10.9897	0.2870	0.4236	0.0105	0.1888	0.0015	2522	24	2277	47	2903	17	22
29-27R	0.02	3.4246	0.0874	0.1067	0.0026	0.2334	0.0015	1510	20	654	15	3069	15	79
29-28C	0.28	13.7353	0.3805	0.5305	0.0140	0.1884	0.0015	2732	26	2744	59	2717	17	-1
29-28R	0.40	1.9080	0.0808	0.0565	0.0023	0.2458	0.0026	1084	28	354	14	3194	14	89
29-29C	0.15	3.3923	0.1022	0.1258	0.0037	0.1962	0.0014	1503	23	764	21	2798	14	73
29-29R *	0.13	4.9745	0.1457	0.1639	0.0043	0.2209	0.0029	1815	24	978	24	2976	22	67

Analysis	Th/U	Radiogenic ratios						Ages (Ma)						% Discordant
		$^{207}Pb/^{235}U$	±	$^{206}Pb/^{238}U$	±	$^{207}Pb/^{206}Pb$	±	$^{207}Pb/^{235}U$	±	$^{206}Pb/^{238}U$	±	$^{207}Pb/^{206}Pb$	±	
29-30C	0.29	12.4676	0.2297	0.4778	0.0081	0.1893	0.0013	2640	17	2518	35	2731	14	8
29-30R *	0.20	11.1335	0.2628	0.4209	0.0086	0.1919	0.0024	2534	22	2264	39	3121	22	27
29-31C *	0.14	6.0071	0.1533	0.2114	0.0051	0.2062	0.0017	1977	22	1236	27	2812	13	56
29-31R *	0.16	9.5951	0.2162	0.3561	0.0072	0.1955	0.0020	2397	21	1964	34	2962	15	34
29-32C *	0.14	14.7681	0.3574	0.4990	0.0115	0.2147	0.0016	2800	23	2609	49	2931	14	11
29-32R *	0.08	6.3096	0.1293	0.2123	0.0038	0.2157	0.0022	2020	18	1241	20	3005	14	59
SAMPLE VGC-41-16														
41-1C	0.31	23.4101	0.5690	0.6539	0.0148	0.2594	0.0020	3244	23	3244	57	3243	12	0
41-1R	0.16	9.9734	0.2636	0.3816	0.0094	0.1894	0.0015	2432	24	2084	44	2737	13	24
41-2C	0.49	14.6943	0.3402	0.5334	0.0114	0.1996	0.0014	2796	22	2756	48	2823	12	2
41-3C *	0.25	4.0922	0.3030	0.1717	0.0126	0.1726	0.0018	1653	59	1022	69	2583	18	60
41-3R	0.17	5.8884	0.1580	0.3117	0.0076	0.1369	0.0014	1960	23	1749	37	2188	18	20
41-4C	0.27	13.4699	0.3474	0.4916	0.0114	0.1985	0.0020	2713	24	2577	49	2814	17	8
41-4R	0.15	13.6595	0.3595	0.4918	0.0120	0.2013	0.0017	2726	25	2578	52	2836	14	9
41-5C	0.67	15.2994	0.4032	0.5492	0.0134	0.2019	0.0018	2834	25	2822	55	2841	14	1
41-5R	0.78	16.3334	0.3784	0.5842	0.0126	0.2026	0.0014	2897	22	2966	51	2847	11	-4
41-6C	0.25	12.6949	0.2402	0.4998	0.0083	0.1826	0.0015	2657	18	2613	36	2677	13	2
41-6R	0.09	6.0449	0.1480	0.3034	0.0069	0.1444	0.0011	1982	21	1708	34	2280	13	25
41-7C	0.29	15.4134	0.2856	0.5789	0.0094	0.1914	0.0015	2841	18	2944	38	2755	13	-7
41-7R *	0.07	38.2434	1.1879	0.5560	0.0125	0.4946	0.0108	3726	30	2850	52	4225	32	33
41-8C *	0.31	21.9250	0.5395	0.5770	0.0133	0.2732	0.0021	3180	24	2936	54	3325	12	12
41-8R *	0.31	75.5811	13.3269	0.4019	0.0597	1.3522	0.1362	4405	163	2178	269	5658	132	62
41-10C *	0.26	37.7556	0.8287	1.0474	0.0208	0.2592	0.0022	3714	21	4619	65	3242	13	-42
41-10R	0.31	14.4294	0.3508	0.5283	0.0116	0.1964	0.0019	2778	23	2734	49	2797	16	2
41-11C	0.03	14.0223	0.2765	0.5480	0.0096	0.1840	0.0015	2751	19	2817	40	2689	13	-5
41-12C	0.43	9.5809	0.2372	0.3903	0.0086	0.1765	0.0019	2395	23	2124	40	2620	18	19

Analysis	Th/U	Radiogenic ratios						Ages (Ma)						% Discordant
		$^{207}Pb/^{235}U$	±	$^{206}Pb/^{238}U$	±	$^{207}Pb/^{206}Pb$	±	$^{207}Pb/^{235}U$	±	$^{206}Pb/^{238}U$	±	$^{207}Pb/^{206}Pb$	±	
41-12R	0.24	10.5687	0.2083	0.4350	0.0077	0.1747	0.0013	2486	18	2328	35	2603	13	11
41-13C	0.28	10.9501	0.1999	0.4674	0.0075	0.1687	0.0013	2519	17	2472	33	2545	13	3
41-14C	0.36	14.6994	0.3266	0.5271	0.0106	0.2008	0.0018	2796	21	2729	45	2833	14	4
41-15C	0.19	12.7625	0.3396	0.4968	0.0118	0.1850	0.0022	2662	25	2600	51	2698	20	4
41-15R	0.27	13.4438	0.2398	0.5102	0.0080	0.1897	0.0014	2711	17	2658	34	2740	12	3
41-16C	0.56	17.8007	0.3387	0.6067	0.0103	0.2113	0.0016	2979	18	3057	41	2915	12	-5
41-17C	0.25	14.6279	0.2754	0.5563	0.0092	0.1893	0.0015	2791	18	2852	38	2737	13	-4
41-17R	0.32	11.3617	0.2261	0.4526	0.0082	0.1808	0.0013	2553	18	2407	36	2660	12	10
41-18C *	0.20	13.9005	0.3183	0.5015	0.0097	0.1996	0.0024	2743	21	2620	42	2823	19	7
41-18R	0.01	5.7714	0.1054	0.3373	0.0055	0.1232	0.0009	1942	16	1874	27	2003	12	6
41-19C *	0.64	49.9651	2.0511	0.6503	0.0244	0.5533	0.0097	3992	40	3229	95	4390	25	26
41-20C	0.22	14.2620	0.2623	0.5576	0.0091	0.1842	0.0014	2767	17	2857	37	2691	13	-6
41-21C *	0.48	48.3930	1.4653	0.7033	0.0187	0.4979	0.0073	3960	30	3433	70	4235	22	19
41-21R	0.28	11.4233	0.1792	0.4531	0.0059	0.1824	0.0014	2558	15	2409	26	2675	13	10
41-22C	0.40	13.3798	0.2186	0.5086	0.0069	0.1904	0.0016	2707	15	2651	29	2745	13	3
41-22R	0.06	12.8944	0.2490	0.4948	0.0079	0.1886	0.0020	2672	18	2591	34	2730	17	5
41-23C	0.40	9.8062	0.1485	0.4089	0.0050	0.1736	0.0013	2417	14	2210	23	2592	13	15
41-23R *	0.18	13.0464	0.2282	0.4727	0.0057	0.1997	0.0025	2683	16	2495	25	2824	20	12
41-24C *	0.52	9.0669	0.2009	0.3694	0.0072	0.1776	0.0018	2345	20	2027	34	2631	17	23
41-24R	0.32	14.7135	0.2288	0.5553	0.0073	0.1917	0.0014	2797	15	2847	30	2757	12	-3
41-25C	0.29	20.8360	0.3272	0.5756	0.0077	0.2619	0.0019	3131	15	2931	31	3258	11	10
41-25R	0.36	25.0636	0.4014	0.6880	0.0093	0.2636	0.0020	3311	16	3375	35	3268	12	-3
41-26C *	0.49	55.9377	2.3485	0.8040	0.0325	0.5015	0.0060	4104	41	3804	115	4246	18	10
41-26R *	0.13	13.9708	0.4165	0.5124	0.0139	0.1965	0.0024	2748	28	2667	59	2798	20	5
41-27C	0.40	16.7451	0.4400	0.5281	0.0128	0.2286	0.0023	2920	25	2733	54	3042	16	10
41-27R *	0.05	14.0989	0.4950	0.4031	0.0103	0.2521	0.0064	2756	33	2183	47	3198	40	32

Analysis	Th/U	Radiogenic ratios						Ages (Ma)						% Discordant
		$^{207}Pb/^{235}U$	±	$^{206}Pb/^{238}U$	±	$^{207}Pb/^{206}Pb$	±	$^{207}Pb/^{235}U$	±	$^{206}Pb/^{238}U$	±	$^{207}Pb/^{206}Pb$	±	
41-28C *	0.32	13.1162	0.3313	0.5100	0.0116	0.1854	0.0020	2688	24	2656	49	2702	18	2
41-28R	0.25	14.1841	0.3097	0.5063	0.0102	0.2020	0.0015	2762	21	2641	44	2842	12	7
41-29C	0.15	12.4607	0.2607	0.4816	0.0092	0.1865	0.0014	2640	19	2534	40	2711	12	7
41-29R *	0.12	16.5970	0.3620	0.5534	0.0107	0.2162	0.0021	2912	21	2839	44	2953	15	4
41-30C *	0.30	15.1869	0.7582	0.3687	0.0123	0.2969	0.0118	2827	46	2023	58	3454	60	41
41-30R	0.26	10.5703	0.2408	0.3780	0.0079	0.2016	0.0017	2486	21	2067	37	2839	13	27
41-31C	0.53	14.2056	0.3268	0.5300	0.0114	0.1933	0.0014	2764	22	2741	48	2771	12	1
41-31R	0.20	13.6550	0.3340	0.5149	0.0118	0.1913	0.0016	2726	23	2677	50	2753	14	3
41-32C	0.24	19.1558	0.5078	0.6285	0.0154	0.2198	0.0022	3050	25	3144	61	2979	16	-6
41-32R	0.20	18.1751	0.4577	0.5980	0.0137	0.2192	0.0023	2999	24	3022	55	2975	16	-2
41-34C	0.83	13.8940	0.3185	0.5133	0.0109	0.1952	0.0015	2743	21	2671	46	2787	13	4
41-34R	0.40	13.8128	0.3274	0.5360	0.0118	0.1859	0.0015	2737	22	2766	49	2706	13	-2
41-35C	0.30	19.3055	0.4712	0.5745	0.0127	0.2424	0.0024	3057	23	2926	52	3136	16	7
41-35R	0.31	16.7190	0.4069	0.5455	0.0124	0.2211	0.0019	2919	23	2806	51	2989	14	6
41-36C	0.40	13.7858	0.3340	0.5272	0.0120	0.1886	0.0015	2735	23	2730	50	2730	13	0
41-36R	0.12	9.3161	0.2193	0.4247	0.0094	0.1582	0.0012	2370	21	2282	42	2437	13	6
41-37C	0.43	13.8001	0.2566	0.5362	0.0089	0.1849	0.0015	2736	17	2768	37	2697	13	-3
41-37R	0.23	19.3406	0.3741	0.5739	0.0099	0.2421	0.0020	3059	19	2924	40	3134	13	7
41-38C	0.46	14.9510	0.2687	0.5656	0.0091	0.1899	0.0014	2812	17	2890	37	2741	12	-5
41-38R *	0.36	11.1359	0.1967	0.4872	0.0077	0.1642	0.0012	2535	16	2559	33	2499	12	-2
41-39C	0.50	17.8143	0.3295	0.6128	0.0101	0.2089	0.0016	2980	18	3081	40	2897	12	-6
41-39R	0.27	16.6231	0.3076	0.5783	0.0096	0.2065	0.0016	2913	18	2942	39	2878	12	-2
41-40C	0.34	14.0876	0.3020	0.4679	0.0089	0.2163	0.0021	2756	20	2474	39	2953	16	16
41-40R *	0.57	12.1697	0.2444	0.4200	0.0071	0.2081	0.0023	2618	19	2261	32	2891	18	22
41-41C *	0.81	12.0855	0.2778	0.4621	0.0083	0.1898	0.0027	2611	21	2449	37	2740	23	11
41-41C *	0.81	34.3793	1.0970	0.7733	0.0162	0.3194	0.0082	3621	31	3693	59	3567	39	-4

Analysis	Th/U	Radiogenic ratios						Ages (Ma)						% Discordant
		$^{207}Pb/^{235}U$	±	$^{206}Pb/^{238}U$	±	$^{207}Pb/^{206}Pb$	±	$^{207}Pb/^{235}U$	±	$^{206}Pb/^{238}U$	±	$^{207}Pb/^{206}Pb$	±	
41-41R	0.49	9.9830	0.1808	0.4318	0.0070	0.1661	0.0012	2433	17	2314	31	2519	12	8
41-42R	0.48	12.6978	0.2194	0.4885	0.0073	0.1886	0.0015	2657	16	2564	31	2730	13	6
41-43C	0.86	9.0783	0.1408	0.3611	0.0044	0.1824	0.0016	2346	14	1987	21	2675	14	26
41-43R *	1.06	8.3751	0.1580	0.3581	0.0059	0.1697	0.0014	2272	17	1973	28	2555	14	23
41-44C	0.46	11.8235	0.1802	0.4720	0.0060	0.1818	0.0013	2591	14	2492	26	2669	12	7
41-44R *	0.13	7.4925	0.1143	0.3549	0.0043	0.1532	0.0013	2172	14	1958	20	2382	14	18
41-45C *	0.69	43.1535	2.0271	0.8443	0.0308	0.3709	0.0116	3846	46	3946	107	3795	46	-4
41-45R *	0.59	11.4929	0.2260	0.3996	0.0060	0.2087	0.0026	2564	18	2167	28	2895	20	25
41-46C	0.40	16.6138	0.2980	0.5623	0.0088	0.2144	0.0017	2913	17	2876	36	2939	12	2
41-46R *	0.01	10.3351	0.2674	0.3587	0.0073	0.2091	0.0034	2465	24	1976	34	2898	26	32
41-47C	0.46	14.4595	0.3249	0.4661	0.0092	0.2242	0.0023	2780	21	2467	40	3011	16	18
41-47R	0.42	12.2409	0.2573	0.4561	0.0079	0.1940	0.0023	2623	20	2422	35	2776	19	13
41-48C	0.63	13.5064	0.2254	0.5045	0.0073	0.1935	0.0014	2716	16	2633	31	2772	12	5
41-48R	0.47	11.8295	0.2372	0.4373	0.0075	0.1955	0.0019	2591	19	2339	34	2789	16	16
41-49C	0.14	13.9440	0.3137	0.5383	0.0105	0.1872	0.0020	2746	21	2776	44	2718	18	-2
41-49R	0.25	11.2648	0.2286	0.4463	0.0079	0.1824	0.0017	2545	19	2379	35	2675	16	11
41-50C *	0.99	24.8527	1.9106	0.4501	0.0101	0.3991	0.0316	3302	72	2396	45	3906	114	39
41-50R	0.49	13.5744	0.2163	0.5149	0.0072	0.1905	0.0012	2720	15	2678	30	2747	11	3
41-51C	0.60	14.0596	0.2577	0.5325	0.0083	0.1908	0.0017	2754	17	2752	35	2749	15	0
41-51R	0.31	11.3262	0.2866	0.4012	0.0089	0.2040	0.0024	2550	23	2175	41	2859	19	24
41-52C	0.34	14.2657	0.2931	0.5274	0.0098	0.1958	0.0016	2768	19	2730	41	2792	13	2
41-52R *	0.24	14.0820	0.3528	0.5376	0.0121	0.1896	0.0021	2755	23	2773	50	2739	18	-1
41-53C	0.26	15.2547	0.2852	0.5750	0.0098	0.1920	0.0012	2831	18	2929	40	2759	11	-6
41-53R	0.22	14.6231	0.3096	0.5373	0.0101	0.1970	0.0018	2791	20	2772	42	2802	15	1
41-54C	0.18	7.9470	0.1850	0.3219	0.0070	0.1787	0.0014	2225	21	1799	34	2641	13	32
41-54R *	0.31	14.0829	0.2994	0.5154	0.0097	0.1978	0.0019	2755	20	2680	41	2808	15	5

Analysis	Th/U	Radiogenic ratios						Ages (Ma)						% Discordant
		$^{207}Pb/^{235}U$	±	$^{206}Pb/^{238}U$	±	$^{207}Pb/^{206}Pb$	±	$^{207}Pb/^{235}U$	±	$^{206}Pb/^{238}U$	±	$^{207}Pb/^{206}Pb$	±	
41-55C	0.22	11.2153	0.2680	0.4605	0.0099	0.1763	0.0018	2541	22	2442	44	2618	17	7
41-55R	0.22	9.7187	0.2050	0.4175	0.0080	0.1685	0.0013	2408	19	2249	36	2543	13	12
41-56C	0.26	16.0888	0.3302	0.5671	0.0107	0.2053	0.0015	2882	19	2896	44	2869	11	-1
41-56R *	0.27	20.8708	0.5137	0.6987	0.0162	0.2162	0.0016	3133	24	3416	61	2953	12	-16
41-57C	0.41	14.6155	0.3357	0.5793	0.0123	0.1847	0.0013	2791	22	2946	50	2695	12	-9
41-57R	0.27	12.3504	0.2935	0.5988	0.0125	0.1510	0.0016	2631	22	3025	50	2357	18	-28
41-58C	0.19	13.6749	0.4195	0.4657	0.0133	0.2149	0.0021	2727	29	2465	58	2943	16	16
41-58R *	0.41	21.0512	0.6102	0.7807	0.0185	0.1974	0.0033	3141	28	3720	67	2804	27	-33
41-59C *	0.24	6.4788	0.1523	0.3110	0.0065	0.1525	0.0015	2043	20	1746	32	2374	16	26
41-59R *	0.18	27.3479	1.2246	0.6469	0.0242	0.3094	0.0079	3396	43	3216	94	3518	39	9
41-61C *	0.47	23.5648	0.6063	0.4503	0.0107	0.3830	0.0034	3251	25	2397	47	3844	13	38
41-61R	0.21	14.3511	0.3319	0.4493	0.0095	0.2338	0.0019	2773	22	2392	42	3078	13	22
41-62C	0.32	12.9712	0.2736	0.5050	0.0097	0.1880	0.0013	2678	20	2635	42	2725	11	3
41-62R	0.34	12.4564	0.2640	0.4817	0.0093	0.1893	0.0013	2639	20	2535	40	2736	12	7

** notes culled analysis*

Appendix E. Biotite schist monazite isotopic data

Analysis	Th/U	Radiogenic ratios						Ages (Ma)						% Discordant
		$^{207}Pb/^{235}U$	±	$^{206}Pb/^{238}U$	±	$^{207}Pb/^{206}Pb$	±	$^{207}Pb/^{235}U$	±	$^{206}Pb/^{238}U$	±	$^{207}Pb/^{206}Pb$	±	
Sample VGC-10-16														
10-1	10.08	12.3680	0.2738	0.4927	0.0089	0.1821	0.0019	2633	21	2582	38	2672	17	3
10-1A	4.48	12.7598	0.2819	0.5098	0.0092	0.1816	0.0018	2662	21	2656	39	2667	17	0
10-1B	10.32	17.7617	0.4138	0.6976	0.0134	0.1847	0.0020	2977	22	3412	51	2695	17	-27
10-2c	4.22	11.9019	0.3131	0.4716	0.0106	0.1830	0.0021	2597	24	2491	46	2681	19	7
10-2r	5.27	12.1970	0.3154	0.4933	0.0106	0.1794	0.0022	2620	24	2585	46	2647	20	2
10-3	4.32	12.2684	0.3161	0.4844	0.0106	0.1837	0.0021	2625	24	2546	46	2687	19	5
10-3A	3.48	12.4099	0.3234	0.4938	0.0109	0.1823	0.0021	2636	24	2587	47	2674	19	3
10-4c	6.43	11.3973	0.2728	0.4556	0.0092	0.1815	0.0019	2556	22	2420	40	2666	17	9
10-4rA	7.06	11.5262	0.2709	0.4600	0.0090	0.1818	0.0019	2567	22	2440	40	2669	17	9
10-4rB	7.29	11.4385	0.2684	0.4569	0.0089	0.1816	0.0019	2560	22	2426	39	2668	17	9
10-4rC	7.29	11.9473	0.2788	0.4817	0.0093	0.1799	0.0019	2600	22	2535	40	2652	17	4
10-4rD	7.63	11.4385	0.2684	0.4569	0.0089	0.1816	0.0019	2560	22	2426	39	2668	17	9
10-4rE	7.63	11.9473	0.2788	0.4817	0.0093	0.1799	0.0019	2600	22	2535	40	2652	17	4
Sample VGC-34-16														
34-1	6.71	12.1451	0.3659	0.4686	0.0132	0.1880	0.0019	2616	28	2477	58	2725	16	9
34-2	4.80	12.8923	0.2219	0.4824	0.0066	0.1939	0.0018	2672	16	2538	29	2775	15	9
34-3	5.32	13.6915	0.4526	0.5249	0.0153	0.1892	0.0030	2729	31	2720	64	2735	26	1
34-4	5.47	13.0709	0.2249	0.5171	0.0072	0.1834	0.0016	2685	16	2687	30	2683	14	0
Sample VGC-42-16														
42-1	2.69	12.7206	0.3108	0.5023	0.0096	0.1837	0.0022	2659	23	2624	41	2687	20	2
42-2	4.48	12.6497	0.2982	0.5046	0.0093	0.1818	0.0021	2654	22	2633	40	2670	19	1
42-3	5.13	12.6672	0.3035	0.5040	0.0095	0.1823	0.0021	2655	22	2631	41	2674	19	2

Analysis	Th/U	Radiogenic ratios						Ages (Ma)						% Discordant
		$^{207}Pb/^{235}U$	±	$^{206}Pb/^{238}U$	±	$^{207}Pb/^{206}Pb$	±	$^{207}Pb/^{235}U$	±	$^{206}Pb/^{238}U$	±	$^{207}Pb/^{206}Pb$	±	
42-4	2.61	12.4907	0.3218	0.4969	0.0102	0.1823	0.0023	2642	24	2600	44	2674	21	3
42-5	3.21	12.4733	0.3144	0.4952	0.0099	0.1827	0.0023	2641	23	2593	42	2677	21	3

Appendix F. Granitic zircon isotope data

Analysis	Th/U	Radiogenic ratios						Ages (Ma)						% Discordant
		$^{207}Pb/^{235}U$	±	$^{206}Pb/^{238}U$	±	$^{207}Pb/^{206}Pb$	±	$^{207}Pb/^{235}U$	±	$^{206}Pb/^{238}U$	±	$^{207}Pb/^{206}Pb$	±	
Sample VGC-23-16														
23-1_5	0.03	9.2685	0.1629	0.4221	0.0068	0.1605	0.0010	2365	16	2270	31	2461	10	8
23-1_6	0.02	7.3404	0.1331	0.3773	0.0062	0.1422	0.0010	2154	16	2064	29	2255	12	8
23-2A_7	0.01	7.1698	0.1254	0.3758	0.0060	0.1395	0.0009	2133	15	2057	28	2221	11	7
23-2A_8 *	0.01	8.9095	0.1783	0.4411	0.0081	0.1476	0.0011	2329	18	2356	36	2319	12	-2
23-2B	0.02	9.7887	0.1733	0.4353	0.0070	0.1644	0.0010	2415	16	2330	32	2501	10	7
23-3A_10	0.01	10.4030	0.1908	0.4631	0.0077	0.1642	0.0011	2471	17	2453	34	2500	11	2
23-3A_11	0.01	9.4517	0.1676	0.4413	0.0072	0.1566	0.0010	2383	16	2356	32	2419	11	3
23-3B	0.15	11.7034	0.2088	0.4927	0.0080	0.1737	0.0011	2581	17	2582	35	2593	10	0
23-4C_5	0.03	10.3076	0.1872	0.4437	0.0074	0.1696	0.0011	2463	17	2367	33	2553	11	7
23-4C_13	0.54	14.3285	0.2586	0.5618	0.0092	0.1865	0.0013	2772	17	2874	38	2711	11	-6
23-5A_9	0.18	13.1644	0.2365	0.5233	0.0086	0.1836	0.0012	2692	17	2713	36	2686	11	-1
23-5A_10	0.25	12.2875	0.2220	0.4898	0.0081	0.1831	0.0012	2627	17	2570	35	2681	11	4
23-5B_6	0.01	8.7453	0.1613	0.4001	0.0067	0.1595	0.0011	2312	17	2170	31	2451	12	11
23-5B_7	0.01	11.3953	0.2020	0.4954	0.0080	0.1679	0.0011	2556	16	2594	34	2537	11	-2
23-5B_8 *	0.01	8.2801	0.1602	0.3943	0.0069	0.1533	0.0012	2262	17	2143	32	2383	13	10
23-6	0.02	12.9425	0.2723	0.4680	0.0090	0.2018	0.0017	2675	20	2475	39	2841	14	13
23-7c	0.43	12.2803	0.2593	0.4806	0.0094	0.1865	0.0014	2626	20	2530	41	2712	13	7
23-7r	0.01	7.5933	0.2245	0.3736	0.0105	0.1483	0.0014	2184	26	2046	49	2327	16	12
Sample VGC-44-16														
44-1	0.04	3.0415	0.0723	0.2178	0.0049	0.1024	0.0007	1418	18	1270	26	1667	12	24
44-2	0.46	6.8618	0.1932	0.3345	0.0088	0.1504	0.0014	2094	25	1860	43	2350	16	21
44-3	0.48	14.2835	0.3337	0.5278	0.0116	0.1984	0.0014	2769	22	2732	49	2813	11	3

Analysis	Th/U	Radiogenic ratios						Ages (Ma)						% Discordant
		$^{207}Pb/^{235}U$	±	$^{206}Pb/^{238}U$	±	$^{207}Pb/^{206}Pb$	±	$^{207}Pb/^{235}U$	±	$^{206}Pb/^{238}U$	±	$^{207}Pb/^{206}Pb$	±	
44-4	0.33	7.2674	0.1842	0.3501	0.0084	0.1522	0.0011	2145	22	1935	40	2370	12	18
44-5A	0.08	7.2381	0.2228	0.3576	0.0101	0.1484	0.0019	2141	27	1971	48	2327	22	15
44-5B	0.15	3.9799	0.1030	0.2440	0.0059	0.1196	0.0010	1630	21	1407	31	1950	14	28
44-6B	0.46	12.3523	0.3075	0.4834	0.0112	0.1873	0.0016	2632	23	2542	49	2719	14	7
44-8	1.84	12.1052	0.2683	0.3853	0.0079	0.2295	0.0020	2613	21	2101	37	3048	14	31
44-9A	0.56	9.8597	0.2264	0.4294	0.0093	0.1683	0.0011	2422	21	2303	42	2541	11	9
44-9B	0.15	7.0798	0.1725	0.3502	0.0081	0.1482	0.0010	2122	21	1936	38	2325	12	17
44-10	0.05	6.6702	0.1363	0.3242	0.0062	0.1503	0.0010	2069	18	1810	30	2349	11	23
44-11 *	0.20	14.7369	0.3310	0.5293	0.0104	0.2034	0.0024	2798	21	2738	44	2853	19	4
44-12	0.33	5.7421	0.1224	0.2964	0.0059	0.1415	0.0010	1938	18	1673	29	2246	13	25
44-13 *	0.16	7.6806	0.1987	0.3180	0.0072	0.1764	0.0025	2194	23	1780	35	2620	24	32
44-14	0.45	4.9077	0.1039	0.2592	0.0051	0.1383	0.0011	1804	18	1486	26	2206	14	33
44-17	0.04	4.8556	0.0923	0.2817	0.0050	0.1259	0.0008	1795	16	1600	25	2041	11	22
44-18	0.02	6.7190	0.1295	0.3247	0.0058	0.1511	0.0010	2075	17	1813	28	2359	11	23
44-19	0.27	7.7553	0.1775	0.3297	0.0068	0.1718	0.0017	2203	20	1837	33	2575	17	29
44-20B	0.16	12.4069	0.2715	0.5008	0.0103	0.1816	0.0011	2636	20	2617	44	2668	10	2
Sample VGC-48-16														
48-1a	0.23	8.4493	0.1779	0.3252	0.0063	0.1885	0.0016	2280	19	1815	31	2729	14	33
48-1b	0.35	12.8980	0.2124	0.4999	0.0073	0.1872	0.0014	2672	15	2613	31	2718	12	4
48-1c	0.22	9.8183	0.1809	0.3601	0.0058	0.1978	0.0019	2418	17	1983	27	2808	16	29
48-1d	0.19	11.3913	0.1881	0.4425	0.0066	0.1868	0.0013	2556	15	2362	29	2714	12	13
48-1e	0.23	11.6570	0.1796	0.4555	0.0062	0.1857	0.0013	2577	14	2420	28	2704	11	11
48-1f	0.25	11.2451	0.1867	0.4323	0.0064	0.1888	0.0014	2544	15	2316	29	2731	12	15
48-1g	0.16	7.3813	0.1203	0.2723	0.0039	0.1967	0.0015	2159	14	1553	20	2799	12	45
48-1h	0.19	12.9309	0.1978	0.5038	0.0068	0.1862	0.0013	2675	14	2630	29	2709	12	3

Analysis	Th/U	Radiogenic ratios						Ages (Ma)						% Discordant
		$^{207}Pb/^{235}U$	±	$^{206}Pb/^{238}U$	±	$^{207}Pb/^{206}Pb$	±	$^{207}Pb/^{235}U$	±	$^{206}Pb/^{238}U$	±	$^{207}Pb/^{206}Pb$	±	
48-1i	0.14	11.3700	0.1988	0.4494	0.0071	0.1838	0.0013	2554	16	2393	32	2688	12	11
48-1j	0.08	9.8204	0.1774	0.3703	0.0060	0.1927	0.0016	2418	17	2031	28	2765	13	27
48-1k *	0.06	8.3468	0.1367	0.3091	0.0044	0.1962	0.0016	2269	15	1737	22	2795	13	38
48-1l	0.09	12.7789	0.2660	0.5117	0.0099	0.1814	0.0014	2663	19	2664	42	2666	13	0
48-2	0.10	12.7085	0.2034	0.4864	0.0069	0.1896	0.0014	2658	15	2555	30	2739	12	7
48-3 *	0.21	14.8196	0.3445	0.4829	0.0103	0.2230	0.0022	2804	22	2540	45	3002	16	15
48-4 *	0.41	24.1746	0.5053	0.5588	0.0107	0.3143	0.0028	3275	20	2862	44	3542	13	19
48-5	0.34	12.7264	0.2528	0.4787	0.0087	0.1931	0.0016	2660	19	2522	38	2769	13	9
48-6	0.44	12.9311	0.1924	0.5228	0.0069	0.1797	0.0012	2675	14	2711	29	2650	11	-2

** notes culled analysis*